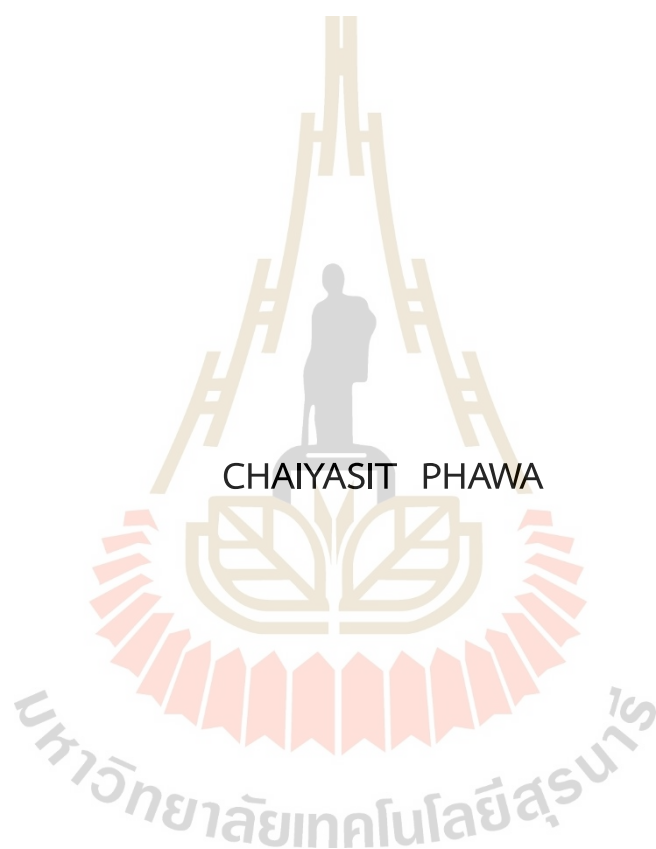


CRYSTAL FACET-CONTROLLED TITANIUM DIOXIDE CATALYSTS
FOR ARTIFICIAL PHOTOSYNTHESIS



A Thesis Submitted in Partial Fulfillment of the Requirements for the
Degree of Doctor of Philosophy in Chemistry
Suranaree University of Technology
Academic Year 2022

ตัวเร่งปฏิกิริยาไทเทเนียมไดออกไซด์ควบคุมผิวหน้าผลึก
สำหรับการสังเคราะห์แสงประดิษฐ์

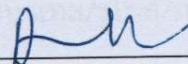


วิทยานิพนธ์นี้เป็นส่วนหนึ่งของการศึกษาตามหลักสูตรปริญญาวิทยาศาสตรดุษฎีบัณฑิต
สาขาวิชาเคมี
มหาวิทยาลัยเทคโนโลยีสุรนารี
ปีการศึกษา 2565

CRYSTAL FACET-CONTROLLED TITANIUM DIOXIDE CATALYSTS FOR ARTIFICIAL PHOTOSYNTHESIS

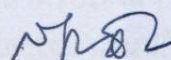
Suranaree University of Technology has approved this thesis submitted in partial fulfillment of the requirements for the Degree of Doctor of Philosophy.

Thesis Examining Committee



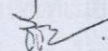
(Assoc. Prof. Dr. Anyanee Kamkaew)

Chairperson



(Assoc. Prof. Dr. Sanchai Prayoonpokarach)

Member (Thesis Advisor)



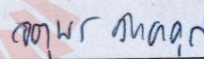
(Dr. Teera Butburee)

Member (Thesis Co-advisor)



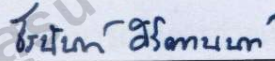
(Dr. Pongtanawat Khemthong)

Member



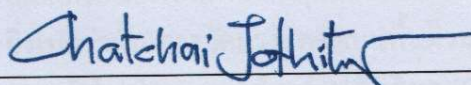
(Prof. Dr. Jatuporn Wittayakun)

Member



(Assoc. Prof. Dr. Theeranun Siritanon)

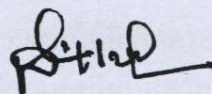
Member



(Assoc. Prof. Dr. Chatchai Jothityangkoon)

Vice Rector for Academic Affairs

and Quality Assurance



(Prof. Dr. Santi Maensiri)

Dean of Institute of Science

ชัยสิทธิ์ ภาวะ : ตัวเร่งปฏิกิริยาไทเทเนียมไดออกไซด์ควบคุมผิวหน้าผลึกสำหรับการสังเคราะห์แสงประดิษฐ์ (CRYSTAL FACET-CONTROLLED TITANIUM DIOXIDE CATALYSTS FOR ARTIFICIAL PHOTOSYNTHESIS) อาจารย์ที่ปรึกษา : รองศาสตราจารย์ ดร.สัญญาชัย ประยูรโภคราช, 65 หน้า.

คำสำคัญ: การแยกน้ำโดยวิธีเคมีไฟฟ้าเชิงแสง/การรีดิวซ์แก๊สคาร์บอนไดออกไซด์โดยวิธีเคมีเชิงแสง (ความร้อน)/ตัวเร่งปฏิกิริยาไทเทเนียมไดออกไซด์/อะนาเทส/รูไทล์/การสังเคราะห์แสงประดิษฐ์

การสังเคราะห์แสงประดิษฐ์ เป็นวิธีที่ได้รับความสนใจสำหรับใช้ในการบรรเทาผลกระทบจากสภาวะโลกร้อน วิธีนี้สามารถผลิตพลังงานสะอาด เช่น แก๊สไฮโดรเจน ผ่านปฏิกิริยาแยกน้ำด้วยวิธีเคมีไฟฟ้าเชิงแสง และยังสามารถลดระดับแก๊สคาร์บอนไดออกไซด์ ผ่านปฏิกิริยารีดิวซ์ได้อีกด้วย สิ่งสำคัญที่ขาดไม่ได้ในกระบวนการเหล่านี้คือ ตัวเร่งปฏิกิริยา โดยทั่วไปสร้างมาจากวัสดุกึ่งตัวนำ ซึ่งหนึ่งในวัสดุกึ่งตัวนำ ที่มีศักยภาพที่จะนำมาสร้างเป็นตัวเร่งปฏิกิริยาคือไทเทเนียมไดออกไซด์ อย่างไรก็ตามยังคงมีอุปสรรคในการนำมาประยุกต์ใช้จริง เนื่องจากไทเทเนียมไดออกไซด์มีแถบพลังงานที่กว้าง การรวมตัวของประจุไฟฟ้าที่รวดเร็ว ความสามารถในการเคลื่อนที่ของประจุไฟฟ้าต่ำและกระบวนการนำกลับมาใช้ใหม่มีค่าใช้จ่ายสูง

วิศวกรรมศาสตร์ของผิวหน้าผลึกถือว่าเป็นวิธีที่มีประสิทธิภาพ สำหรับการชะลอการรวมตัวของประจุไฟฟ้า การเพิ่มความจำเพาะต่อปฏิกิริยาเคมี และการส่งเสริมการเคลื่อนที่ของประจุไฟฟ้าในเทคโนโลยีสังเคราะห์แสงประดิษฐ์ อย่างไรก็ตาม ผลกระทบของผลึกไทเทเนียมไดออกไซด์ที่ไม่ได้ควบคุมผิวหน้าผลึกยังคงคุมเครือ งานวิจัยนี้จึงได้สังเคราะห์ตัวเร่งปฏิกิริยาแบบฟิล์มที่มีไทเทเนียมไดออกไซด์เป็นหลัก โดยควบคุมผิวหน้าผลึกอย่างเป็นระบบบนแผ่นนำไฟฟ้าของทินออกไซด์ที่เจือด้วยพลูออรีนโดยวิธีไฮโดรเทอร์มอล สำหรับประยุกต์ใช้ในปฏิกิริยาแยกน้ำด้วยวิธีเคมีไฟฟ้าเชิงแสง และปฏิกิริยารีดิวซ์แก๊สคาร์บอนไดออกไซด์ด้วยวิธีเคมีเชิงแสง การปลูกผลึกไทเทเนียมไดออกไซด์บนแผ่นนำไฟฟ้าโดยตรงนี้ สามารถเพิ่มความสามารถในการถ่ายเทประจุไฟฟ้า และการนำตัวเร่งปฏิกิริยากลับมาใช้ใหม่ ฟิล์มอะนาเทสที่สังเคราะห์ควบคุมคู่หน้าผลึกที่อัตราส่วนแตกต่างกันนำมาใช้เป็นขั้วแอโนดสำหรับปฏิกิริยาแยกน้ำด้วยวิธีเคมีไฟฟ้าเชิงแสง จากผลการทดลองพบว่า ตัวเร่งปฏิกิริยาที่มีคู่หน้าผลึกแบบ {101}-{001} เมื่อฉายแสงจะมีค่ากระแสไฟฟ้าและประสิทธิภาพของโฟตอนต่อกระทบต่อกระแสไฟฟ้าเพิ่มขึ้นตามปริมาณของหน้าผลึก {001} ซึ่งถือได้ว่าเป็นด้านที่มีพลังงานพื้นผิวสูง สำหรับตัวเร่งปฏิกิริยา {010}-{001}-1 ที่มีคู่หน้าผลึกแบบ {010}-{001} ซึ่งมีเปอร์เซ็นต์หน้าผลึก {001} น้อยที่สุด ผลการทดลองนี้เกิดจากการที่หน้าผลึก {010} นั้นมีอิเล็กตรอนอัมฟิโนตีที่ต่ำที่สุดซึ่งบ่งบอกว่าหน้าผลึก {010} สามารถให้อิเล็กตรอนแก่ขั้วแคโทดได้ดีกว่า ยิ่งไปกว่านั้น การวัดแรงยึดติดบนพื้นผิวของตัวเร่งปฏิกิริยาด้วยเทคนิคไมโครสโกปีแรงอะตอมชนิดวัดการนำไฟฟ้า พบว่าตัวเร่งปฏิกิริยา {010}-{001}-1 มีแรงยึดติดบนพื้นผิวสูงที่สุด ซึ่งบ่งบอกถึงประสิทธิภาพของตัวเร่งปฏิกิริยาในการดูดซับน้ำเพื่อที่จะเกิดปฏิกิริยาออกซิเดชันโดยโซลไดทันที่ ผลการทดลองนี้แสดงให้เห็นถึงความสำคัญของอิเล็กตรอนอัมฟิโนตีและความสามารถในการดูดซับน้ำ

CHAIYASIT PHAWA : CRYSTAL FACET-CONTROLLED TITANIUM DIOXIDE CATALYSTS FOR ARTIFICIAL PHOTOSYNTHESIS. THESIS ADVISOR : ASSOC. PROF. SANCHAI PRAYOONPOKARACH, Ph.D. 65 PP.

Keyword: PHOTOELECTROCHEMICAL WATER SPLITTING/PHOTO-THERMAL CO₂ REDUCTION/TiO₂-BASED CATALYSTS/ANATASE/RUTILE/ARTIFICIAL PHOTOSYNTHESIS

Artificial photosynthesis (AP) is a promising approach for mitigating the effects of global warming. It enables the production of green energy in the form of hydrogen through photoelectrochemical (PEC) water splitting and contributes to reducing CO₂-levels via the CO₂ reduction reaction (CO₂RR). One of the most important parts of these methods is catalysts, usually made from semiconductors. Among various semiconductor materials, TiO₂ holds great potential for photocatalyst fabrication. However, it faces challenges such as a wide band gap, rapid charge recombination, low charge carrier mobility, and high reusability costs.

Crystal facet engineering has been widely recognized as a potent methodology for effectively suppressing charge recombination, enhancing chemical selectivity and promoting charge transfer in AP technology. However, the effects of TiO₂ crystal with arbitrarily tunable facet has been ambiguous. In this study, facet-controlled TiO₂-based catalysts were systematically synthesized on fluorine-doped tin oxide (FTO) substrates using a hydrothermal method for applications in PEC water splitting and photochemical CO₂RR. The direct growth of TiO₂ crystals on FTO substrates encourages charge transportation and the catalyst's reusability. Facet-controlled anatase films with different facet ratios were employed as photoanodes for PEC water splitting. The experimental results revealed that films with a higher percentage of the {001} facet recognized as a high surface energy facet, particularly in the {101}-{001} facet pair, exhibited higher photocurrents and incident photon-to-current efficiency (IPCE). Among the facet pairs, {010}-{001}-1, which had the lowest {001} facet percentage, demonstrated the best performance in PEC water splitting. This observation can be attributed to the {010} facet possessing the lowest electron affinity, indicating its superior ability to provide electrons to the cathode. Furthermore, conductive atomic force microscopy (CAFM) measurements revealed the highest adhesive force on the {010}-{001}-1 surface, suggesting its effective adsorption of water molecules that can be readily oxidized by holes. The findings emphasize the significance of the electron affinity and water adsorption ability of the films in reducing

electron-hole recombination and achieving high photocurrents. The synthesized films also exhibited excellent stability over a 6-hour irradiation period, indicating their potential for practical applications in solar-driven catalysis.

For the photo-thermal CO₂ reduction activity using rutile with {110}-{001} facet over anatase films as the catalyst, rutile demonstrates a higher rate of CO₂ reduction. Rutile may exhibit higher CO₂ adsorption energy, facilitating the further reduction of CO molecules to CH₄ through multiple proton-coupled electron transfer (PCET) steps. Conversely, anatase releases CO molecules upon their formation, resulting in 100% selectivity of CO production. Enhanced CO₂ reduction performance of rutile can also be attributed to its lower band gap, enabling efficient light absorption and charge carrier generation. While increasing the reaction temperature boosts CO₂ reduction product yields, selectivity remains unchanged, indicating temperature primarily affects kinetics rather than reaction pathways. Moreover, the PCET process is more efficient at higher temperatures, further enhancing CO₂ reduction performance. Employing dual wavelengths at 370 nm (ultraviolet region) and 870 nm (infrared region) suggests that the infrared heat increases the reaction temperature rather than directly excited TiO₂. While CO₂ adsorption is crucial for TiO₂-based CO₂ reduction, water adsorption is also important because it serves as a vital hole scavenger and proton source. Hence, controlling the TiO₂ phase, water content, and reaction temperature are promising strategies for enhancing future TiO₂-based photo-thermal CO₂ reduction systems.

School of Chemistry
Academic Year 2022

Student's Signature _____
 Advisor's Signature _____
 Co-advisor's Signature _____

ACKNOWLEDGEMENTS

I am sincerely thankful to Assoc. Prof. Dr. Sanchai Prayoonpakarach, my thesis advisor, for his guidance and continuous support throughout the research process from the beginning of my Ph.D. journey. I also would like to thank him for not giving up on me for 7 years of my study. I would like to extend my heartfelt appreciation to Dr. Teera Butburee, my thesis co-advisor, for the experiences in photocatalysis research.

I am grateful to the members of my thesis committee, Dr. Pongtanawat Khemthong, Prof. Dr. Jatuporn Wittayakun, Assoc. Prof. Dr. Theeranun Siritanon and Asst. Prof. Dr. Anyanee Kamkaew. Their expertise, feedback, and suggestions have been invaluable in improving the quality of this thesis.

I would like to express my deepest appreciation to Tawin Phawa, Kwanta Phawa and my family for their unwavering support, understanding, and encouragement throughout this journey. I am also grateful to Kaewklao Pradublai, my girlfriend. Their love, patience, and belief in my abilities have been a constant source of motivation.

I would like to acknowledge Suranaree University of Technology, NANOTEC (a member of the National Science and Technology Development Agency), and Jagiellonian University in Poland for their support in research facilities, and access to academic databases has been invaluable in conducting this research. I would like to express my gratitude to all the participants in NANOTEC, Jatuporn and Sanchai groups for their participation in this study.

I would love to show appreciation to unforgettable memories with Dr. Nattawut Osakoo and Jutamas Osakoo who always give me a lot of invaluable advice. Dr. Chalermpan Keawkumay and Chaianun Pansakdanon who were beside me on the memorable night. I would like to thank Prof. Wojcech Macyk and Photocatalysis team for wonderful research visit experiences in Jagiellonian University. I would like to thank Dr. Kasidid Yaemsunthorn and Nuttagarn Yaemsunthorn, they are my everything and make me feel like I am home through our traditional songs during research visit in Poland. Additionally, I am grateful to Somphon Chamontree and Chanaporn Akkharin for their willing help and support in Poland. Lastly, I would like to acknowledge any other individuals, organizations, or sources that have directly or indirectly contributed to this thesis in any way but may not have been explicitly mentioned.

Chaiyasit Phawa

CONTENTS

	Page
ABSTRACT IN THAI.....	I
ABSTRACT IN ENGLISH.....	III
ACKNOWLEDGEMENTS.....	V
CONTENTS.....	VI
LIST OF TABLES.....	VIII
LIST OF FIGURES.....	IX
CHAPTER	
I INTRODUCTION.....	1
1.1 Significance of the study.....	1
1.2 Research objectives.....	5
1.3 Scope and limitations of the study.....	6
II LITERATURE REVIEW.....	7
2.1 Photocatalytic properties of TiO ₂	7
2.2 Artificial Photosynthesis (AP).....	12
2.3 Water splitting on semiconductor photocatalysts.....	14
2.3 Carbon dioxide reduction reaction (CO ₂ RR).....	17
III EXPERIMENTAL.....	23
3.1 Chemicals.....	23
3.2 Preparation of clean FTO substrate.....	24
3.3 Preparation of TiO ₂ on FTO substrate.....	24
3.4 Characterization of catalysts.....	25
3.5 Incident photon to charge carrier efficiency of catalysts.....	25
3.6 Intensity-modulated photocurrent spectroscopy of samples.....	25

CONTENTS (Continued)

		Page
	3.7 PEC water splitting performance measurements.....	26
	3.8 Photo CO ₂ RR catalytic performance measurements.....	26
IV	RESULTS AND DISCUSSION.....	27
	4.1 PEC water splitting by anatase TiO ₂	27
	4.1.1 Synthesis of anatase TiO ₂ films.....	27
	4.1.2 PEC water splitting activities.....	35
	4.2 CO ₂ photo-thermal reduction reaction by rutile and anatase TiO ₂	45
	4.2.1 Synthesis of rutile and anatase TiO ₂ films.....	45
	4.2.2 Photo-thermal CO ₂ reduction activity.....	48
V	CONCLUSIONS.....	53
	REFERENCES.....	56
	CURRICULUM VITAE.....	65

LIST OF TABLES

Table		Page
2.1	Half electrochemical thermodynamic reactions of the main ECR production, and their corresponding standard redox potentials [V versus reversible hydrogen electrode (RHE)] (Fan et al., 2020).....	19
3.1	Chemicals used in this research.....	23
3.2	The synthesis conditions for preparing TiO ₂ on FTO substrate.....	24
4.1	The band gap energy, surface area per cm ² , and facet percentages of crystal samples.....	30
4.2	Total electron affinity of anatase TiO ₂	42



LIST OF FIGURES

Figure	Page
1.1 Evolution of global temperature (black), atmospheric CO ₂ concentration (red), CO ₂ concentration in air trapped in Antarctic ice cores (green) and solar activity (yellow) from 1920 to 2020. Data were taken from the website RealClimate: Climate Science from Climate Scientists [http://www.realclimate.org/]. This graphic was produced using the climate widget at this URL: [http://herdsoft.com/climate/widget/].	2
2.1 Schematic demonstration of selective photodeposition of Ag and MnO ₂ on TiO ₂ films with different facets (a). SEM images showing Ag photodeposition (b-d) and MnO ₂ photodeposition (e-g). Reprinted (adapted) with permission from (Butburee et al., 2019). Copyright 2019 Royal Society of Chemistry.	9
2.2 Calculated relative band edges of the {101} and {001} facets of anatase TiO ₂ . CBM and VBM are the conduction band minimum and valence band maximum, respectively. Reprinted (adapted) with permission from (Liu et al., 2016). Copyright 2016 American Chemical Society.	10
2.3 Possible directions of charges transfer between rutile and anatase. Reprinted (adapted) with permission from (Buchalska et al., 2015). Copyright 2015 American Chemical Society.	11
2.4 A schematic representation of the molecular machinery that catalyses' oxygenic photosynthesis. Reprinted (adapted) with permission from (Jones and Fyfe, (2001) Copyright 2001 Current Biology.	13
2.5 Schematic energy diagram of photocatalytic water splitting for (a) one-step and (b) two-step photoexcitation. Reprinted (adapted) with permission from (Hisatomi, Kubota, and Domen, 2014). Copyright 2014 Royal Society of Chemistry.	14

LIST OF FIGURES (Continued)

Figure	Page
4.1 SEM images showing the morphology of single-crystalline anatase TiO ₂ , a-c) {101}-{001} facets with different {101}/{001} facet ratios and d-e) {010}-{001} facets with different {010}/{001} facet ratios. Reprinted (adapted) with permission from (Phawa et al., 2021). Copyright 2021 ChemCatChem.	27
4.2 XRD patterns of anatase TiO ₂ with a) {101}-{001} and b) {010}-{001} facet pairs. Reprinted (adapted) with permission from (Phawa et al., 2021). Copyright 2021 ChemCatChem.	29
4.3 Raman spectra of anatase TiO ₂ with a) {101}-{001} and b) {010}-{001} facet pairs. Reprinted (adapted) with permission from (Phawa et al., 2021). Copyright 2021 ChemCatChem.	31
4.4 Surface area estimation of 106 μm ² scanned area based on AFM. Reprinted (adapted) with permission from (Phawa et al., 2021). Copyright 2021 ChemCatChem.	32
4.5 UV-Vis absorption spectra of anatase TiO ₂ with a) {101}-{001} and b) {010}-{001} facet pairs. Reprinted (adapted) with permission from (Phawa et al., 2021). Copyright 2021 ChemCatChem.	33
4.6 Tauc plots of anatase TiO ₂ with a) {101}-{001} and b) {010}-{001} facet pairs. Reprinted (adapted) with permission from (Phawa et al., 2021). Copyright 2021 ChemCatChem.	34
4.7 The PEC water splitting performance of anatase TiO ₂ with a) {101}-{001} and b) {010}-{001} facet pairs. Reprinted (adapted) with permission from (Phawa et al., 2021). Copyright 2021 ChemCatChem.	36
4.8 IPCE of anatase TiO ₂ with a) {101}-{001} and b) {010}-{001} facet pairs. Reprinted (adapted) with permission from (Phawa et al., 2021). Copyright 2021 ChemCatChem.	37

LIST OF FIGURES (Continued)

Figure	Page
4.9 Photocurrents generated by various samples tested under the simulated sunlight (AM 1.5) for 6 hr at the applied voltage of 0.6 V vs Ag/AgCl. Reprinted (adapted) with permission from (Phawa et al., 2021). Copyright 2021 ChemCatChem.....	38
4.10 The EIS spectra of anatase TiO ₂ with a) {101}-{001} and b) {010}-{001} facet pairs. Reprinted (adapted) with permission from (Phawa et al., 2021). Copyright 2021 ChemCatChem.....	40
4.11 IMPS spectra of anatase TiO ₂ with a) {101}-{001} and b) {010}-{001} facet pairs. Reprinted (adapted) with permission from (Phawa et al., 2021). Copyright 2021 ChemCatChem.....	41
4.12 Adhesion force of anatase TiO ₂ surface with a) {101}-{001} and b) {010}-{001} facet pairs. Reprinted (adapted) with permission from (Phawa et al., 2021). Copyright 2021 ChemCatChem.....	44
4.13 SEM images showing the morphology of single-crystalline of a) rutile and b) anatase TiO ₂	45
4.14 XRD patterns of synthesized rutile and anatase TiO ₂	46
4.15 Diffuse reflectance spectra of rutile and anatase TiO ₂	47
4.16 Tauc plots of rutile and anatase TiO ₂	47
4.17 a) Homemade gas-phase reactor and b) the irradiation set up.....	48
4.18 Products from photo-thermal CO ₂ reduction using rutile and anatase TiO ₂ catalysts under 370 nm light irradiation for 6 h.....	49
4.19 Relative CO production of different dual wavelengths using anatase as a catalyst.....	51
4.20 Relative CO production of different water temperatures using anatase TiO ₂ as a catalyst.....	52

CHAPTER I

INTRODUCTION

1.1 Significance of the study

Carbon dioxide (CO₂) is one of the greenhouse gases involved in the global warming. Figure 1 illustrates a concerning trend of dramatically increased CO₂ concentration in the atmosphere over the past 50 years. Since 2000, human activities such as transportation, industrial fossil fuel combustion, and agricultural practices have been responsible for an annual rise in CO₂ levels of 1 to 2 ppm. This increase in CO₂ concentration has been correlated with a rise in global temperature.

Since the Earth's system composes of many subsystems, changes in one system can impact the others. For example, rising global temperature led to ice melting in the Earth's polar regions. Consequently, the reflection of light from the sun by polar ice was reduced, leading to more light absorption on the Earth's surface and increasing global temperature (Allan, Hawkins, Bellouin, and Collins, 2021). This phenomenon is global warming which causes climate change and directly impacts human health (both physical and mental health) via natural and human systems, including economic and social conditions and disruptions (Pörtner et al., 2022).

The slight increase in global temperature has many serious effects on our planet more than several people expected. Greenhouse gases (GHGs) from human activities contribute significantly to global warming besides energy from the sun and natural GHGs. Because of the development of several countries, global energy consumption has been rapidly increasing every year. Especially in 2018, energy consumption grew by +2.9%, the fastest since 2010 (Dudley, 2018). Moreover, the main consumed energy is still fossil fuels resulting in the increase of emissions of GHGs such as CO₂, methane (CH₄), and nitrous oxide (N₂O). The average temperature of the earth's surface and oceans are proportionally increased with the level of these GHGs because they can trap infrared radiation emitted from the earth's surface and sun light. (Moore, Heilweck, and Petros, 2021; Yoro and Daramola, 2020; Zandalinas, Fritschi, and Mittler, 2021).

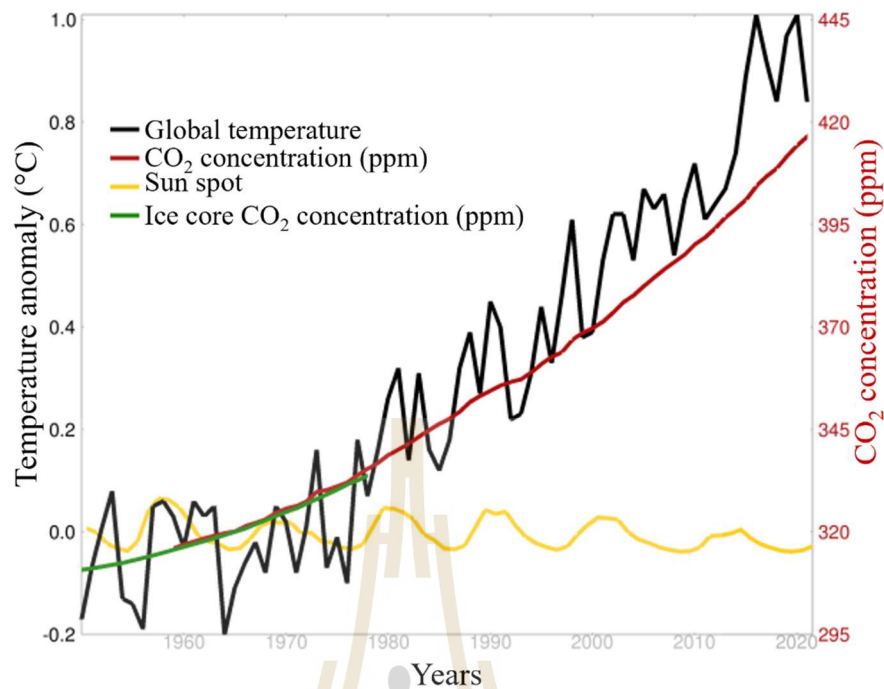


Figure 1.1 Evolution of global temperature (black), atmospheric CO₂ concentration (red), CO₂ concentration in air trapped in Antarctic ice cores (green) and solar activity (yellow) from 1920 to 2020. Data were taken from the website RealClimate: Climate Science from Climate Scientists [<http://www.realclimate.org/>]. This graphic was produced using the climate widget at this URL: [<http://herdsoft.com/climate/widget/>].

Accordingly, in December 2015, 195 nations made the Paris Agreement at the 21st Conference of the Parties (COP21), focusing on taking into account holding the increase in the global average temperature to well below 2 °C and chasing efforts to limit the temperature increase to 1.5 °C above pre-industrial levels by controlling the CO₂ emission (Agreement, 2015). As mentioned before, global warming has to be considered a critical problem due to it causes many adverse effects such as large floods, extreme weather changes, sea level rise, heavier monsoons or drought in some areas, less drinking water, and ocean acidification (Prakash, 2021). Hence, addressing the reduction of GHG concentrations, particularly CO₂, is a critical issue that demands significant attention. In order to tackle the challenge of high CO₂ concentrations, two key strategies are proposed: the substitution of fossil fuels with hydrogen (H₂) and the implementation of CO₂ reduction measures.

Among many CO₂ reduction and H₂ production technologies, AP is considered a fascinating candidate. AP is the simulated natural photosynthesis that utilizes abandoned sunlight to produce high energy chemicals. This strategy naturally converts

CO₂ into carbohydrates and splits water into O₂ and H₂ under sunlight via CO₂ reduction and water splitting. Therefore, AP is an attractive strategy to overcome global warming effects since it can be applied to produce H₂ energy via PEC water splitting reaction without any greenhouse gas production and reduce CO₂ level via photocatalytic carbon dioxide reduction reaction (CO₂RR). Generally, one of the most important parts of this system is semiconductor photocatalysts to catalyze the reactions. Among many semiconductors, titanium dioxide (TiO₂) is a potential and practical semiconductor due to its high thermal and chemical stability, environmentally benign, and low-cost production. However, TiO₂ has large band gap energy, 3.2 eV, which causes a high recombination rate of electron-hole pairs and retards the overall reactions. Consequently, the design and development of TiO₂-based materials are crucial in this research field.

TiO₂ has been widely studied in many applications since its PEC activity was first discovered in 1972 (Fujishima and Honda, 1972). The unique properties of TiO₂ lead to many possible applications, for example, N₂-to-NH₃ reduction (Wu et al., 2019), degradation of antibiotics (Li, Jia, Shao, and He, 2019) or organic dye molecules (Lee, Kim, Choi, Chung, and Han, 2019), cancer treatment (Chu et al., 2019) and H₂ production (Hejazi et al., 2019). In photocatalysis, when TiO₂ absorbs UV radiation matching its band gap energy, charge separation of electrons and holes occurs. These charge carriers could contribute to redox reactions under suitable conditions. Charge transport of the charge carriers is one of the critical factors affecting the overall photocatalytic performance of TiO₂. Docampo, Guldin, Steiner, and Snaith (2013) revealed that the grain boundary of TiO₂ particles could trap free electrons resulting in electron transport suppression. Therefore, faster electron transport could be obtained from less grain boundary.

To achieve effective charge transport, Cho et al. (2011) prepared TiO₂ nanorods on fluorine-doped tin oxide (FTO) substrate to reduce the charge transport limitation from TiO₂ grain boundaries and the contact area between TiO₂ and FTO substrate. The researchers found that the measured incident photo-to-current efficiency (IPCE) of single crystalline branched TiO₂ nanorods on the FTO substrate was 67%, whereas that of TiO₂ nanoparticles on the FTO substrate was only 6%. One of the possible causes of the different IPCE values might be the different formation of TiO₂ on the FTO substrate. TiO₂ nanoparticles were deposited on the FTO substrate by screen printing the particles on the substrate. The particles randomly contacted the substrate surface resulting in high charge transport suppression. On the contrary, the single crystalline

TiO₂ nanorods directly grown on the FTO substrate by a sol-gel process could promote better charge transportation.

Recently, Butburee et al. (2019) hydrothermally grew single crystalline TiO₂ on an FTO substrate. They found that TiO₂ crystal facets could be precisely controlled by adjusting F⁻ ions, H⁺ concentration, time, and reaction temperature. Moreover, the study revealed that the high surface energy facet, e.g., {001} facet, was favorable for water oxidation. TiO₂ with the highest {001} facet percentage provided the highest water oxidation performance. However, TiO₂ with a high portion of {001} facet does not always provide better photocatalytic performance (Chamtouri et al., 2017; Hu et al., 2014; Chuanhao Li et al., 2015; Wu, Liu, Wu, Li, and Piao, 2012; Zhang et al., 2018). A suitable portion of co-exposed facets has been reported to influence the photocatalytic activity of TiO₂ (Liu et al., 2016; Yu, Low, Xiao, Zhou, and Jaroniec, 2014). However, a systematic study of precise tuning of co-exposed facets and their effect on photocatalytic performance is rare. Therefore, in this work, the synthesis of anatase TiO₂ with low-index facet pairs, {101}-{001} and {010}-{001}, with fine-tuning of the facet ratio, was investigated. The obtained products with different ratios of co-exposed facets were characterized and tested for their photocatalytic activity in PEC water splitting.

TiO₂, without any modification, is also recognized as a poor catalyst for CO₂RR (Lan, Xie, Chen, Hu, and Cui, 2019). High energy is needed to break the strong bonds between C and O to generate a CO intermediate. The binding of CO₂ and the intermediate on the catalyst surface is the key to achieving significant CO₂RR performance. Excessive binding energy leads to strong adsorption on the catalyst surface, hindering the release of the products. In contrast, weak binding energy causes less adsorbed reactants on the catalyst surface, resulting in a lower product yield. The influences of the adsorption between intermediate molecules and the catalyst's surface on CO₂RR performance were also reported in the case of Cu-based catalyst, which has considered one of the most selective catalysts (Gao et al., 2019; Jeong et al., 2019; Ma et al., 2020).

The rutile TiO₂ with {110}-{001} facet has been reported to exhibit stronger CO₂ adsorption on its surface compared to the anatase phase (Kovačič, Likozar, and Huš, 2022). The researchers calculated the adsorption energy between CO₂ molecules and TiO₂ surfaces of anatase and rutile phase and found that weak interactions between CO₂ and anatase surfaces implied physisorption. In contrast, strong CO₂ adsorption was observed on {001} rutile surfaces, with CO₂ molecules adopting a bent configuration upon adsorption. The C_{CO₂} atom bonded to the O_{rutile} atom, while the O_{CO₂} atom

bonded to the Ti_{rutile} atom. As a result, the CO_2 molecule was readily deformed. The distance between the CO_2 molecule and the rutile surface was shorter than that of the anatase, facilitating charge transfer from the rutile surface to the CO_2 molecule. Moreover, strong CO_2 binding at the TiO_2 surface is not the only critical factor; the efficient diffusion of product molecules from the surface and the influx of new CO_2 molecules to the surface is also important. Photo energy has been coupled with thermal energy to facilitate molecular diffusion at the catalyst surface, resulting in improved product yield and selectivity (Li, Zhang, Huang, Xu, and Zhang, 2021; Wang et al., 2020; Xu et al., 2018).

Given these findings, anatase with different facet ratios and facet pairs ($\{001\}$ - $\{101\}$ and $\{001\}$ - $\{010\}$) has been prepared for the PEC water splitting reaction. The catalysts were tested in a 3-electrode system under simulated solar light. The effects of facet ratio, facet pairs, charge transportation, electron affinity, and hole accumulation were reported. In the case of photo- CO_2RR , $\{110\}$ - $\{001\}$ rutile has been primarily investigated over anatase as the catalyst. Reactions were conducted in a gas-phase system under UV irradiation at 370 nm. The reaction temperature was varied from 25 °C to 80 °C using a water bath. Finally, the effects of temperature and catalyst properties were compared to anatase.

1.2 Research objectives

The research objectives were as follows:

1. To develop TiO_2 -based materials for the water splitting and carbon dioxide reduction reactions.
2. To synthesize TiO_2 with different facet pairs on FTO substrate for PEC water splitting and photo-thermal CO_2RR .
3. To explain the photoactivities of the synthesized catalyst PEC water splitting and photo- CO_2RR reactions.

1.3 Scope and limitations of the study

The scope and limitations of the study are listed:

1. Single-crystalline rutile and anatase TiO_2 with various percentages of facet pairs were synthesized on FTO substrates.
2. The percentages of facet pairs were adjusted by the concentration of HCl.
3. $\{101\}$ - $\{001\}$ and $\{010\}$ - $\{001\}$ facet pairs were controlled by the concentration of ammonium hexafluorotitanate.
4. PEC water splitting performance of anatase was investigated through photocurrent measurement in 1 M NaOH solution under simulated solar light irradiation.
5. Photo-thermal CO_2RR by rutile was performed via a homemade gas phase reactor under UV irradiation at 370 nm.
6. The effects of anatase facet pair on PEC water splitting were evaluated.
7. The rutile and anatase phase effects on photo-thermal CO_2RR were investigated.
8. The quantities of CO_2RR products were analyzed by gas chromatography (GC).
9. Morphology and electronic properties of synthesized catalysts on FTO substrate were characterized by X-ray diffraction (XRD), scanning electron microscopy (SEM), Raman spectroscopy, UV-Vis absorption spectroscopy, Diffuse reflectance spectroscopy, conductive atomic force microscopy (CAFM) and electrochemical impedance spectroscopy (EIS).

CHAPTER II

LITERATURE REVIEW

2.1 Photocatalytic properties of TiO₂

TiO₂ is among the most common semiconductors used in photocatalysis. It has a large band-gap energy, 3.0 – 3.2 eV, allowing it to absorb the UV radiation of the wavelength <390 nm. The basic building block of TiO₂ is composed of 6 oxygen atoms surrounding 1 titanium atom in a distorted octahedral configuration. Crystals of TiO₂ exist in three major forms: rutile, anatase, and brookite, depending on the arrangement of TiO₆ octahedral units.

Single crystalline TiO₂ particles usually show greater performance in photocatalytic activities than amorphous TiO₂ particles (Cho et al., 2011; Docampo, Guldin, Steiner, and Snaith, 2013). The defects in TiO₂ particles could act as recombination sites and result in lower photocatalytic performance. Anatase TiO₂ has been reported to have much higher activity than other TiO₂ structures (Bakardjieva, Šubrt, Štengl, Dianez, and Sayagues, 2005). The performance of various crystalline catalysts is also highly dependent on their crystal facets. Hence, the design and development of crystal facets have been introduced to optimize the performance by finely tuning the surface atomic configuration and coordination (Pan, Liu, Lu, and Cheng, 2011).

Low-index facet anatase TiO₂ is composed of three different crystal facets, which are {001}, {010}, and {101} (Liu et al., 2016). The surface free energies of {001}, {010}, and {101} facets are 0.96, 0.68, and 0.49 J/m², respectively (Yan, Chen, and Jing, 2019). The crystal with higher surface free energy usually reveals excellent catalytic performance compared to the lower ones. However, the total surface free energy is minimized during the crystal growth process resulting in the decrease of the highly reactive facet, {001} facet (Yang et al., 2008).

The density, size, and surface chemistry of the resulting crystalline nucleus are dependent on solution matrices during the formation processes; therefore, the growth rate and orientation of crystals can be finely controlled by adjusting the solution compositions (Dinh, Nguyen, Kleitz, and Do, 2009). Yang et al. (2008) investigated the effects of absorbed atoms at the crystal surface on the growth of {001} facet. The addition of hydrofluoric acid (HF) as a fluoride (F⁻) source could not only decrease the total surface free energy of crystal but also yield the highest percentage of {001} facet

(47%). Dinh et al. (2009) reported the effects of the solution ratio between oleic acid (OA) and oleylamine (OM), which act as a capping surfactant in the synthesis of TiO_2 . They found that OA limited the growth direction along {001} facet resulting in a higher percentage of {001} facet and thinner crystals. OM inhibited the direction growth along {101} facet resulting in the presence of a higher percentage of {101} facet. Shiu et al. (2012) and Roy et al. (2014) also reported similar results when they used a base, diethylamine (DEA) as a shape controller. These reports show that F^- content and the acid-base environments of the solutions influenced the existence of {001} facet.

Recently, Butburee et al. (2019) reported factors that affected the structure of single-crystalline anatase TiO_2 during synthesis processes. TiO_2 was hydrothermally synthesized on fluorine-doped tin oxide (FTO) conductive substrate by adjusting the composition of chemicals, which are water, hydrochloric acid (HCl) as a source of H^+ , ammonium fluorotitanate (AFT) as a F^- source, and titanium-butoxide (TTBT) as a Ti^{4+} source. Moreover, the reaction time and temperature were also studied. The effects of each factor are as follows:

1. water/HCl composition

The increase of HCl content caused the higher {001} facet percentage and thinner crystal. Nevertheless, the crystal could not be attached to the FTO substrate if the HCl content was further increased.

2. F^- content

F^- resulted in an anatase phase transformation instead of a rutile phase formation due to F^- reduced total surface energy of anatase more than the rutile phase. Besides, the crystal size increased with the amount of F^- . Therefore, F^- act as both crystal phase transformation and structure reconstruction.

3. Ti^{4+} content

The crystal size was extended following the increase of Ti^{4+} content in the growth solution.

4. Reaction time and temperature

Longer reaction time and higher temperature led to higher crystallinity along with an increase in the crystal size.

Furthermore, the study also revealed the selectivity of each facet. {001} facet was favorable for the oxidation reaction as proved by Mn^{2+} oxidation, but {101} and {010} facets preferred the reduction reaction as proved by Ag^+ reduction as shown in Figure 2.1. These phenomena indicated that holes were transferred to {001} facet and electrons were simultaneously transferred to {101} and {010} facets after light illumination (Roy, Sohn, and Pradhan, 2013; Ye, Liu, Tian, Peng, and Zan, 2013; Ye, Mao,

et al., 2013; Yu et al., 2014; Zhang et al., 2018). Liu et al. (2016) calculated the relative band structure of {101} and {001} facets to explain the charge transportation. As shown in Figure 2.2, the conduction band potential of {101} facet is less positive than that of {001} facet, but the valence band potential of {101} facet is more negative than that of {001} facet. Generally, electrons and holes prefer to locate at lower positive and negative band potentials, respectively. Consequently, electrons and holes were respectively transferred to the conduction band of {101} facet and the valence band of {101} facet.

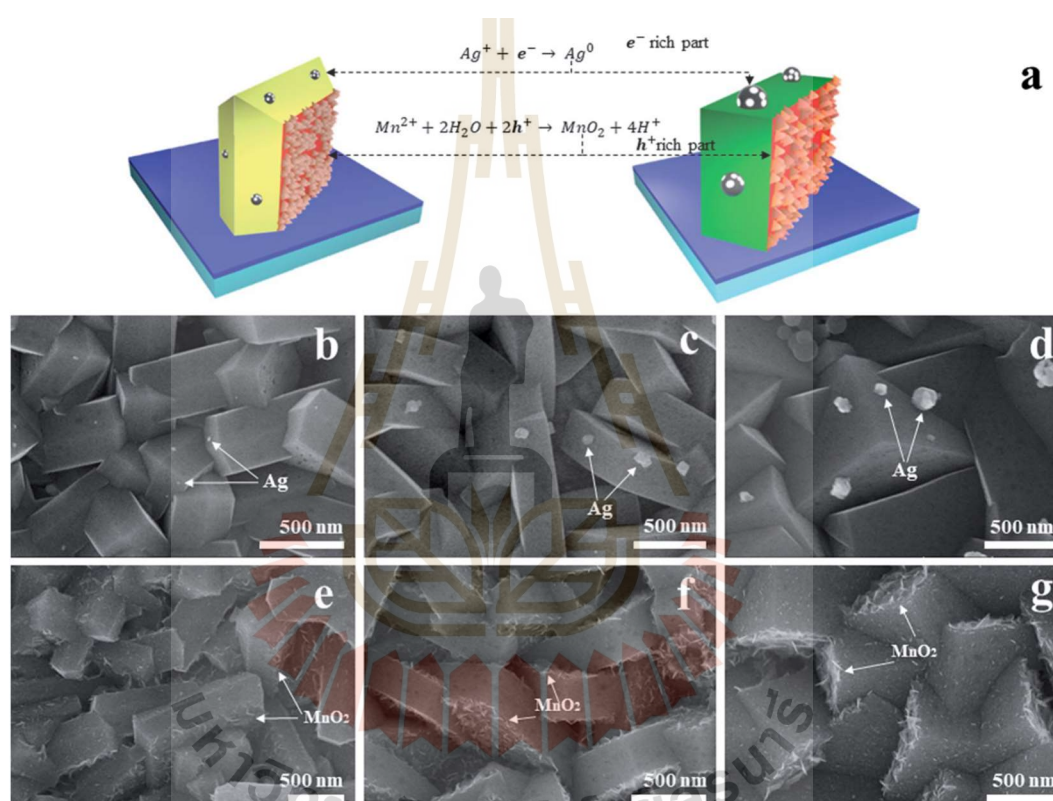


Figure 2.1 Schematic demonstration of selective photodeposition of Ag and MnO₂ on TiO₂ films with different facets (a). SEM images showing Ag photodeposition (b-d) and MnO₂ photodeposition (e-g). Reprinted (adapted) with permission from (Butburee et al., 2019). Copyright 2019 Royal Society of Chemistry.

The increase of the highly reactive facet, {001} facet, should significantly raise the photocatalytic performance of the oxidation reaction (Butburee et al., 2019; Wu et al., 2012) when the crystal size was uniform. However, some reports conflicted with this finding (Li et al., 2015; Zhang et al., 2018; Zheng et al., 2011). When the exceed independent facet was exposed on the crystal, the charge transportation was not

balanced. The excess charge carriers overflowed to the unfavorable facet resulting in high charge recombination. Moreover, Li et al. (2015) observed the behaviors of anatase TiO₂ with various facet percentages on PEC performance. They revealed that the performance was not dependent on only the surface energy but also the compatibility of the photocatalyst and the reactant resulting in the higher performance of the electrode with higher percentages of {010} facet instead of {001} facet.

From the above literature, several researchers have focused on the anatase phase of TiO₂ because rutile usually shows lower photocatalytic activity. Moreover, the synergistic effects, anatase/rutile composites (e.g., P25), show better performance than both bare anatase and rutile TiO₂. Hence, P25 is commonly used as a standard material for TiO₂-based catalysts.

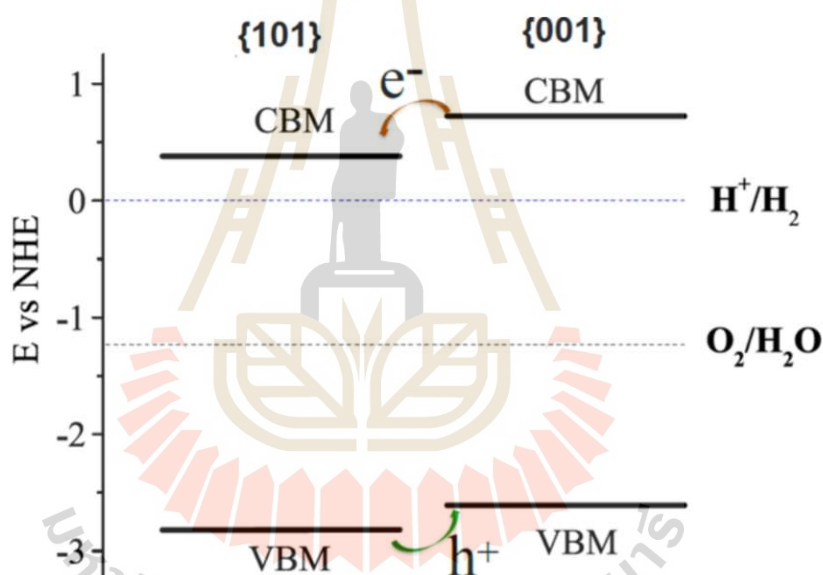


Figure 2.2 Calculated relative band edges of the {101} and {001} facets of anatase TiO₂. CBM and VBM are the conduction band minimum and valence band maximum, respectively. Reprinted (adapted) with permission from (Liu et al., 2016). Copyright 2016 American Chemical Society.

Concerning the band alignment of rutile and anatase, Mi and coworker proposed five potential band alignments for rutile and anatase composites (Mi and Weng, 2015). However, Buchalska et al. (2015) and Scanlon et al. (2013) suggested that electron transfer primarily occurs from the rutile CB to the anatase CB rather than through other processes. As illustrated in Figure 2.3, hydroxyl radicals (OH[•]) are generated through the reduction of H₂O₂ and the oxidation of H₂O. Their findings indicate that superoxide ions

($\text{O}_2^{\cdot-}$) form readily at both rutile and anatase sites due to the reduction of O_2 and the oxidation of H_2O_2 , respectively. Furthermore, the results highlight that the hydroxyl radical yield is the highest compared to anatase and P25. Given that the conduction and valence bands of rutile are higher than those of anatase, the authors suggest that rutile functions as a more potent reducer and a weaker oxidant than anatase. These observations were similar to Yaemsunthorn's work (Yaemsunthorn, Kobielsuz, and Macyk, 2021).

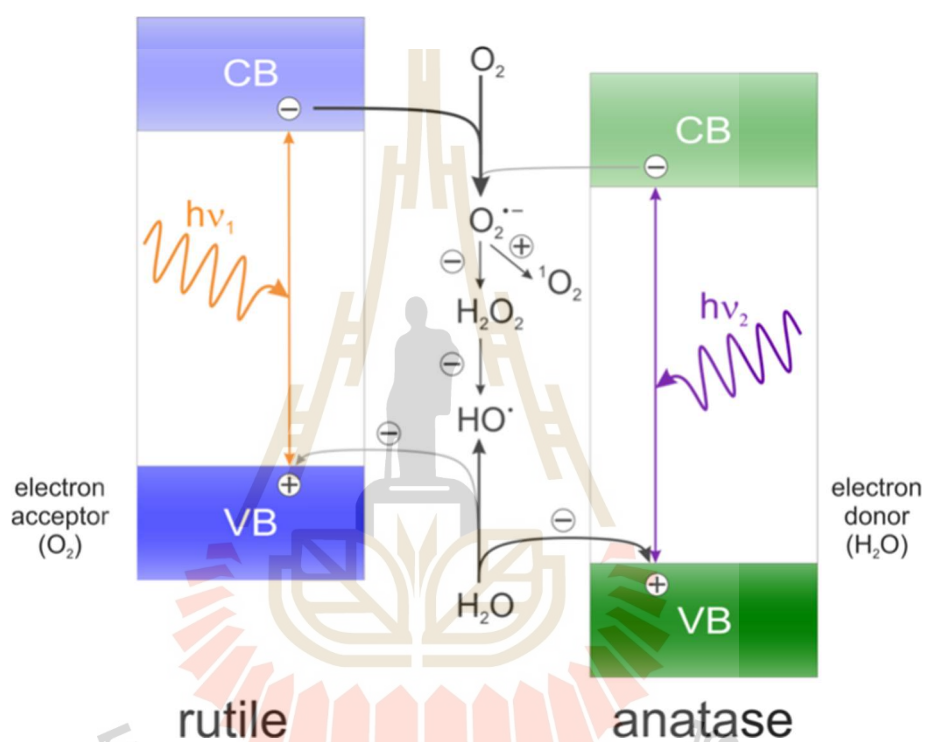


Figure 2.3 Possible directions of charges transfer between rutile and anatase. Reprinted (adapted) with permission from (Buchalska et al., 2015). Copyright 2015 American Chemical Society.

2.2 Artificial Photosynthesis (AP)

Amidst the ongoing energy consumption crisis, various clean and renewable green technologies have emerged. One of these innovations is AP, drawing inspiration from natural photosynthesis, a process where CO_2 and H_2O are transformed into carbohydrates like glucose while releasing O_2 as a byproduct under sunlight energy (Barber and Tran, 2013; Das, 2021; Perathoner and Centi, 2020). Within the realm of AP, scientists and researchers aim to replicate this natural phenomenon using human-made materials and devices. The ultimate goal is to convert sunlight into chemical energy, such as hydrogen or other alternative fuels, instead of producing glucose. This approach presents a promising avenue for sustainable energy production and mitigating the impact of greenhouse gas emissions.

The concept of AP can be likened to the photosynthesis process in plant leaves. Jones and Fyfe (2001) explained that natural photosynthesis involves two key components: Photosystem I (PSI) and Photosystem II (PSII), as depicted in Figure 2.4. In PSII, chlorophylls and other pigments act as reaction centers that capture light energy from the sun. This absorbed energy then excites electrons within the chlorophyll molecules situated at the reaction center. One of the crucial steps in PSII is water splitting, which involves a water oxidation reaction leading to the production of O_2 . Additionally, this process generates four protons and four electrons in plastoquinone. These electrons are subsequently transferred to plastocyanin, a small, water-soluble copper protein, through an integral membrane protein known as the cytochrome *b_f* complex. As the process continues, these electrons are utilized to reduce carbon dioxide during the Calvin cycle, resulting in the production of glucose. This fascinating mechanism of AP mimics the photosynthesis process found in nature, clearing the way for harnessing sunlight to drive chemical reactions and potentially generate alternative fuels such as H_2 for sustainable energy solutions.

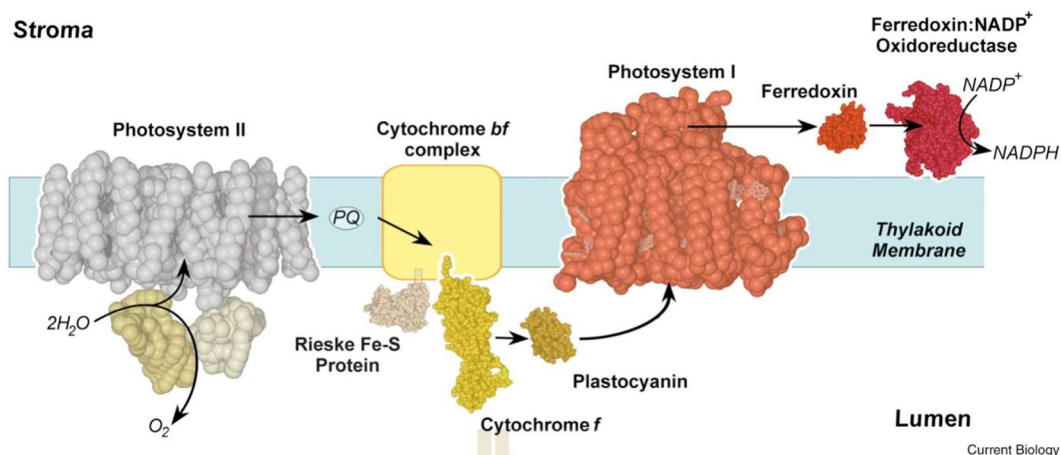


Figure 2.4 A schematic representation of the molecular machinery that catalyses' oxygenic photosynthesis. Reprinted (adapted) with permission from (Jones and Fyfe, 2001) Copyright 2001 Current Biology.

Research in the field of artificial photosynthesis encompasses diverse approaches, ranging from the development of specialized photocatalysts and photoelectrodes to the integration of light-absorbing materials and catalysts, all aimed at facilitating the chemical reactions involved in the conversion process. Although the technology is still in its early stages, ongoing advancements show promising potential for a greener and more sustainable energy future. In this particular study, facet-controlled TiO_2 crystals were employed to emulate the functionalities of artificial leaves (AL). These crystals acted as catalysts for photoelectrochemical (PEC) water splitting and photo CO_2 reduction reactions. A detailed literature review was conducted to explore the photoactivity of TiO_2 in both water splitting and CO_2 reduction processes, providing valuable insights for this study. The use of facet-controlled TiO_2 crystals offers several benefits, enhancing the efficiency and selectivity of the photoconversion reactions. Understanding and leveraging these crystals' properties is expected to advance the field of artificial photosynthesis and contribute to the development of sustainable energy solutions.

2.3 Water splitting on semiconductor photocatalysts

Clean, renewable, and sustainable energy sources as an alternative to fossil fuels have been extensively investigated. H_2 has received much attention because it has the highest energy density. Besides, it is storable, transportable, and can be converted into electricity (Dudley, 2018). H_2 can be produced from many sources such as natural gas and coal, via a gas reforming process. However, a cleaner and environmentally friendly process to produce H_2 could be from a water splitting reaction.

Overall water splitting reaction, $H_2O(l) \rightarrow H_2(g) + 1/2O_2(g)$, is not a thermodynamically spontaneous reaction. The standard Gibbs free energy change (ΔG) of this reaction is +238 kJ/mol (Peter et al., 2016). Using photocatalysts could reduce the energy barrier and make this reaction possible. Generally, the water splitting reaction can be operated via two different approaches. One approach is directly splitting water into H_2 and O_2 using a single photocatalyst, as shown in Figure 2.5a. However, this approach needs the photocatalyst, which has a suitable band gap energy matching the redox potentials to reduce H^+ to H_2 and oxidize H_2O to O_2 .

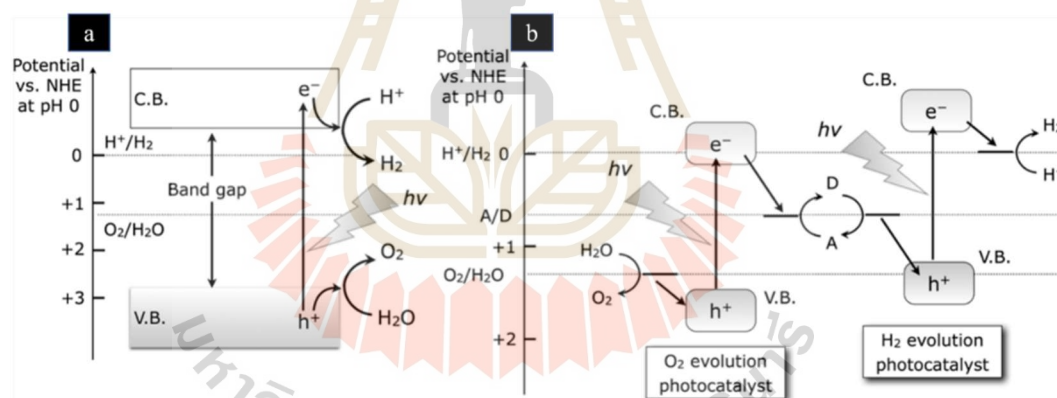


Figure 2.5 Schematic energy diagram of photocatalytic water splitting for (a) one-step and (b) two-step photoexcitation. Reprinted (adapted) with permission from (Hisatomi, Kubota, and Domen, 2014). Copyright 2014 Royal Society of Chemistry.

The other approach is to apply two excitation steps using two different photocatalysts and an electron mediator. The approach is simulated from natural photosynthesis and is known as Z-scheme (Hisatomi et al., 2014). In the Z-scheme system, as shown in Figure 2.5b, one photocatalyst is used to oxidize water to produce O_2 . Another photocatalyst is responsible for the reduction of H^+ to produce H_2 . This system uses a redox couple, an electron acceptor (A), and an electron donor (D) as an

electron mediator. The photogenerated electrons from the first photocatalyst can reduce A to D. Then, D can reduce the photogenerated holes from the second photocatalyst. The Gibbs free energy can be changed by adjusting the steps of the photoexcitation system. Also, using visible light for the photocatalyst excitation is possible with this approach.

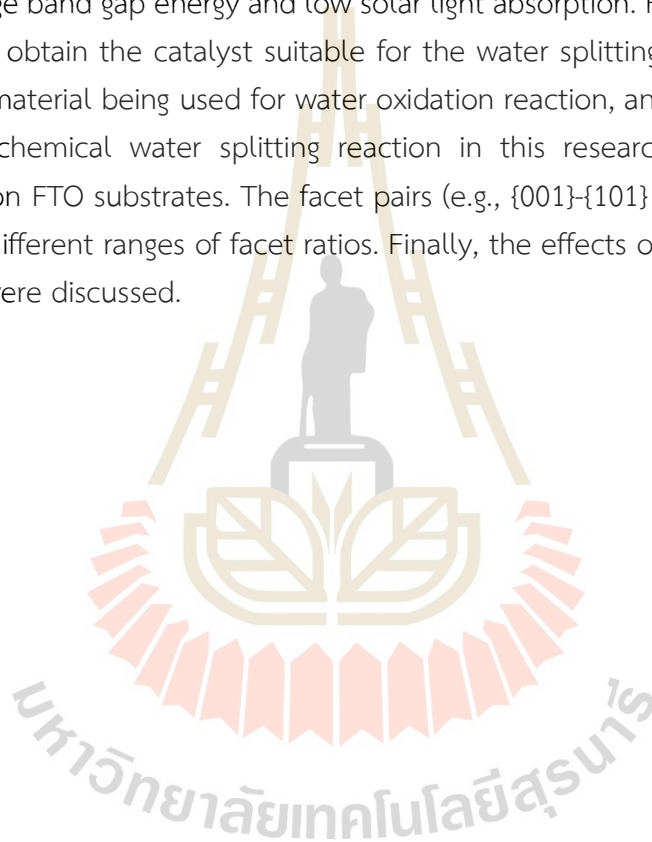
Three steps are involved in the overall water splitting reaction on semiconductor photocatalysts. The first step is the light absorption of the photocatalyst with photon energy \geq the band gap energy to generate electron-hole pairs. The second step is the separation and migration of the photogenerated charge carriers from the bulk material to the surface. The third step is the reduction of H^+ to H_2 and the oxidation of H_2O to O_2 by the photogenerated electrons and holes, respectively. The structure and electronic properties of the photocatalyst influence the first two steps. High photocatalytic performance tends to be achieved from the photocatalysts with high crystallinity and those with nanosize particles. The third step could be improved by a co-catalyst.

Many photocatalysts were synthesized for the water splitting reaction such as IrO_x /black Si (Kan, Qian, Zhang, Yue, and Zhao, 2017), N-doped Co/ β - Mo_2C on carbon nanotube (Ouyang, Ye, Wu, Xiao, and Liu, 2019), hierarchical Co-Fe oxyphosphide microtube (Zhang, Lu, Nai, Zang, and Lou, 2019) and PtS- $ZnIn_2S_4$ nanosheets loaded on WO_3 (Ding et al., 2019). They are good candidates for the water splitting reaction. However, they have some drawbacks; for example, photocorrosion in aqueous environments, unsuitable CB levels for the reduction, low charge mobility, and fast charge recombination. Some photocatalysts were prepared via complicated strategies. Therefore, photocatalysts with simple synthesized routes such as TiO_2 , which is one of the promising candidates for PC and PEC applications, has been extensively studied. However, TiO_2 without any modification is not effective enough for practical use.

Wang et al. (2011) prepared rutile TiO_2 nanowires (H: TiO_2) by annealing pristine TiO_2 in H_2 atmosphere. From overall IPCE measurement, H: TiO_2 performance was improved by three orders of magnitude compared to the bare rutile TiO_2 in the UV region. These results corresponded with Pt/ TiO_2 nanosheet with exposed {001} facets synthesized by Yu et al. (2010) that the reaction was performed in ethanol solution. Pt was deposited in {001} facets to accept the excited electrons from the conduction band to prevent the direct charge recombination of electrons and holes. Therefore, the H_2 production rate of Pt/ TiO_2 was dramatically higher than the bare TiO_2 . Another noble metal- TiO_2 catalyst was also prepared to overcome TiO_2 limitation. Gogoi, Namdeo, Golder, and Peela (2020) synthesized Ag-doped TiO_2 for solar energy

harvesting to produce H_2 . The light absorption range was extended and the band gap energy was reduced to 2.5 eV when Ag was doped. The photocurrent density of Ag/TiO₂ was improved about 4 times. Besides, a non-metal element such as C was also doped into the TiO₂ structure to increase the utilization of solar light in the visible region (Park, Kim, and Bard, 2006). The performance was considerably increased by 25 times higher than P-25 film under white-light illumination. The increase in performance was also obtained with B-doped TiO₂ nanotubes (Li, Lu, Quan, Chen, and Zhao, 2008).

As mentioned above, bare TiO₂ was hardly used for the water splitting reaction due to its large band gap energy and low solar light absorption. Hence, optimizing TiO₂ properties to obtain the catalyst suitable for the water splitting reaction is essential. Due to TiO₂ material being used for water oxidation reaction, anatase was focused on photoelectrochemical water splitting reaction in this research. Anatase TiO₂ was synthesized on FTO substrates. The facet pairs (e.g., {001}-{101} and {001}-{010}) were prepared in different ranges of facet ratios. Finally, the effects of facet pairs and facet percentage were discussed.



2.3 Carbon dioxide reduction reaction (CO₂RR)

CO₂ is well-known as one of the major greenhouse gases causing global warming effects. Human activities are not the only cause of CO₂ emission but also natural sources such as the respiration of living organisms and wildfire. However, human activities such as fossil fuel burning, deforestation, industrial processes, and agriculture contribute significantly.

When CO₂ is released into the atmosphere, it can absorb and re-desorb infrared radiation, which is heat energy. The heat is trapped in the atmosphere and consequently warms the earth. The more CO₂ concentration, the higher the global temperature would be raised. The effects of global temperature rising are widespread and can be seen in many events of the natural world including melting ice caps and glaciers, rising sea levels, increasing the number and intensity of heatwaves, droughts, and extreme weather changes. Furthermore, these events can have serious consequences for human societies and ecosystems, including food and water insecurity.

The increase in greenhouse gas concentrations, especially CO₂, has negatively affected living organisms. Reducing emitted CO₂ from human activities should be taken seriously. There are several ways to reduce CO₂ emissions such as using renewable energies (i.e., wind, solar, and hydropower), reducing meat consumption, and using low-carbon transportation. Moreover, improving energy efficiency or using clean energy such as H₂ is important. H₂ can be produced from zero-carbon emission process (i.e., water splitting reaction) and release zero-carbon after combustion.

Several measures including reducing emissions, improving energy efficiency, reforestation, and direct air capture, should be performed simultaneously to reduce the amount of CO₂ in the atmosphere. CO₂ can be stored after combustion using absorption, adsorption, or membrane separation technologies (post-combustion capture). For example, Chehrazhi and Moghadas (2022) revealed that the new Chilled Ammonia Process (CAP) technology could recover CO₂ from ammonia plants and reuse it in a urea plant. CAP technology converted CO₂ into chemical fertilizers, further promoting agricultural product yields. In addition, CO₂ can also be stored before the combustion process is finished, called pre-combustion capture. These processes are performed through gasification and water gas shift reactions to convert CO and H₂O to H₂ and CO₂. Then, H₂ is used as a clean fuel and CO₂ is further separated and stored (Chen and Chen, 2020). However, many challenges still need to be addressed, including the high cost of capture technologies, the need for reliable storage sites, and the environmental impacts of long-term storage.

Besides the above measures, CO₂ level can be parallelly deducted by converting to valuable chemicals via catalytic reaction (i.e., CO₂RR). The reduction of CO₂ to valuable chemicals and fuels not only produces sustainable energy but also directly decreases CO₂ levels. Several products, such as CH₄, formic acid (HCOOH), CO, and ethylene (C₂H₄), can be formed through various pathways depending on several factors, including the type of catalyst, reaction conditions, and strategies. Conversion of CO₂ into value-added chemicals is still challenging because CO₂ is relatively stable with a strong C=O bond (750 kJmol⁻¹).

CO₂RR involves complex multi-electron/proton transfer processes with different possible reaction intermediates and products. Half-electrochemical thermodynamic reactions and standard redox potentials for various products are summarized in Table 2.1. CO₂ first undergoes adsorption and interaction with atoms on the catalyst surface to form *CO₂⁻, followed by various stepwise transfers of protons (typically derived from water oxidation) and/or electrons toward different final products. The formation of the CO₂ intermediate is regarded as a controlling step in the overall reaction of CO₂ reduction at the catalyst surface. Subsequently, local rate-determining steps (RDSs) occur in distinct pathways for each product, further influencing the reaction dynamics and products. For instance, CH₄ formation can occur through the pathways: CO₂ → *COOH → *CO → *CHO → *CH₂O → *CH₃O → CH₄ + *O → CH₄ + *OH → CH₄ + H₂O (Fan et al., 2020; Khezri, Fisher, and Pumera, 2017).

Among many photocatalysts, TiO₂ catalysts have attracted significant attention for their potential to catalyze the conversion of CO₂ into CO₂RR products. However, the efficient conversion of CO₂ in CO₂RR using TiO₂ catalysts remains challenging. Modification of TiO₂ catalysts through doping or surface functionalization has been shown to enhance their activity towards CO₂RR. For example, incorporating transition or noble metals such as Cu, Ag, and Ni into TiO₂ catalysts has significantly improved their CO₂RR activity. The bimetallic dimer-embedded anatase (101) surface, consisting of Zn-Cu, Zn-Pt, or Zn-Pd, was also demonstrated to be suitable for the adsorption of CO* and O intermediates, which subsequently facilitated the reduction and promotion of CO₂RR performance (Li et al., 2022).

Table 2.1 Half electrochemical thermodynamic reactions of the main ECR production, and their corresponding standard redox potentials [V versus reversible hydrogen electrode (RHE)] (Fan et al., 2020).

Products	Acid		Base	
	Equation	E(V)	Equation	E(V)
Hydrogen	$2\text{H}^+ + 2\text{e}^- \rightarrow \text{H}_2$	0.000	$2\text{H}_2\text{O} + 2\text{e}^- \rightarrow \text{H}_2 + 2\text{OH}^-$	-0.828
Carbon monoxide	$\text{CO}_2 + 2\text{H}^+ + 2\text{e}^- \rightarrow \text{CO} + \text{H}_2\text{O}$	-0.104	$\text{CO}_2 + \text{H}_2\text{O} + 2\text{e}^- \rightarrow \text{CO} + 2\text{O}$	-0.932
Methane	$\text{CO}_2 + 8\text{H}^+ + 8\text{e}^- \rightarrow \text{CH}_4 + 2\text{H}_2\text{O}$	0.169	$\text{CO}_2 + 6\text{H}_2\text{O} + 8\text{e}^- \rightarrow \text{CH}_4 + 8\text{OH}^-$	-0.659
Methanol	$\text{CO}_2 + 6\text{H}^+ + 6\text{e}^- \rightarrow \text{CH}_3\text{OH} + \text{H}_2\text{O}$	0.016	$\text{CO}_2 + 5\text{H}_2\text{O} + 6\text{e}^- \rightarrow \text{CH}_3\text{OH} + 6\text{OH}^-$	-0.812
Formic acid	$\text{CO}_2 + 2\text{H}^+ + 2\text{e}^- \rightarrow \text{HCOOH}$	-0.171	$\text{CO}_2 + \text{H}_2\text{O} + 2\text{e}^- \rightarrow \text{HCOO}^- + \text{OH}^-$	-0.639
Ethylene	$2\text{CO}_2 + 12\text{H}^+ + 12\text{e}^- \rightarrow \text{C}_2\text{H}_4 + 4\text{H}_2\text{O}$	0.085	$2\text{CO}_2 + 8\text{H}_2\text{O} + 12\text{e}^- \rightarrow \text{C}_2\text{H}_4 + 12\text{OH}^-$	-0.743
Ethane	$2\text{CO}_2 + 14\text{H}^+ + 14\text{e}^- \rightarrow \text{C}_2\text{H}_6 + 4\text{H}_2\text{O}$	0.144	$2\text{CO}_2 + 10\text{H}_2\text{O} + 14\text{e}^- \rightarrow \text{C}_2\text{H}_6 + 14\text{OH}^-$	-0.685
Ethanol	$2\text{CO}_2 + 12\text{H}^+ + 12\text{e}^- \rightarrow \text{CH}_3\text{CH}_2\text{OH} + 3\text{H}_2\text{O}$	0.084	$2\text{CO}_2 + 9\text{H}_2\text{O} + 12\text{e}^- \rightarrow \text{CH}_3\text{CH}_2\text{OH} + 12\text{OH}^-$	-0.744
Acetic acid	$2\text{CO}_2 + 8\text{H}^+ + 8\text{e}^- \rightarrow \text{CH}_3\text{COOH} + 2\text{H}_2\text{O}$	0.098	$2\text{CO}_2 + 5\text{H}_2\text{O} + 8\text{e}^- \rightarrow \text{CH}_3\text{COO}^- + 7\text{OH}^-$	-0.653
n-Propanol	$3\text{CO}_2 + 18\text{H}^+ + 18\text{e}^- \rightarrow \text{CH}_3\text{CH}_2\text{CH}_2\text{OH} + 5\text{H}_2\text{O}$	0.095	$3\text{CO}_2 + 13\text{H}_2\text{O} + 18\text{e}^- \rightarrow \text{CH}_3\text{CH}_2\text{CH}_2\text{OH} + 18\text{OH}^-$	-0.733

It has been reported that the TiO_2 {001} and {101} surface junctions could efficiently convert CO_2 into CH_4 with a high yield rate of $1.35 \text{ mmol g}^{-1} \text{ h}^{-1}$. Furthermore, co-exposure of {100} and {001} facets could lead to a particular CO_2 product, CH_3OH ,

at a yield rate of $1.5 \text{ mmol g}^{-1}\text{h}^{-1}$ (Jiang et al., 2020). The Zeeman-effect-assisted anodic oxidation method was utilized to synthesize TiO_2 to obtain the crystals with various exposure ratios of the {100} crystal facet. An increase in the exposure ratio of the {100} crystal facet led to an increase in the yield of $\text{C}_2\text{H}_5\text{OH}$, while the formation of CH_4 was suppressed. This finding is attributed to the promotion of the connection of CO^* intermediates rather than their rapid desorption to CO . Notably, the connection of CO^* intermediates represents the rate-determining step of the reaction.

Moreover, the heterojunction of the composites between TiO_2 and metal oxide has also been introduced to improve charge separation. Hybrid copper oxide-titanium dioxide ($\text{Cu}_x\text{O-TiO}_2$) heterostructure composites were synthesized for photocatalytic CO_2 reduction. The inherent p-n heterojunction of the synthesized catalyst significantly enhanced light absorption and charge separation, resulting in a high CH_4 yield of $221.63 \text{ ppmg}^{-1}\text{h}^{-1}$ (Park et al., 2016). Lei et al. (2018) reported that CO_2 could be reduced to CO with the highest yield of $2.4 \text{ } \mu\text{molg}^{-1}$ using TiO_2 crystals featuring a {001}/{101} facet pair on carbon nanofibers under simulated sunlight. The researchers proposed that the surface junction between the {001} and {101} facets facilitated electron-hole separation and extended light absorption, which, in turn, further enhanced the photocatalytic activity.

Not only charge separation of the catalyst is important to CO_2RR but also CO_2 adsorption-desorption efficiency. Li et al. (2021) documented that the Ag/MgO -modified surface of TiO_2 augmented the adsorption of CO_2 and exhibited favorable desorption-adsorption characteristics for key CO_2RR intermediates, CO^* , HCOOH^* , HCHO^* , and CH_3OH^* , which is imperative for C_1 product selectivity. Additionally, the combination of Au and MgO facilitated electron transfer between the key intermediates and the catalyst surface, resulting in a substantial increase in CH_4 selectivity (Li et al., 2021). Cu_2O nanowires coated with a Cu^+ -incorporated TiO_2 overlayer have been shown that the presence of Cu^+ in the TiO_2 layer not only improved charge transport but also functioned as an adsorption site for CO_2 molecules, exhibiting a high binding energy of 240 kJmol^{-1} . Consequently, the faradaic efficiency (FE) of the modified catalyst reached 56.5%, which is significantly higher than that of the bare Cu_2O nanowire (23.6%) (Park et al., 2016). In addition, hierarchical TiO_2 nanorods with a highly active {001} surface exhibit superior properties in terms of light absorption and surface area. The synergistic effects of the active surface increase the charge transfer along the nanorods, resulting in significantly enhanced production of methane (CH_4) and methanol (CH_3OH) compared to P25, a commonly used form of TiO_2 (Cao et al., 2019).

To increase CO₂ adsorption, Crake et al. (2019) synthesized composites of TiO₂ and metal-organic framework (MOF) (NH₂-UiO-66), resulting in highly porous materials. The CO yield under UV-visible light was found to be nine times higher than that of bare TiO₂. The success of this approach can be attributed to the introduction of NH₂-UiO-66 into the TiO₂ catalyst, which led to improved charge separation and light absorption. Furthermore, the number of CO₂ adsorption sites dramatically increased, enabling stronger binding with CO₂ molecules and their subsequent reduction to CO with 100% selectivity.

The study conducted by Neatu et al. (2014) also confirmed the crucial role of intermediates adsorption. Au-Cu nanoalloys were incorporated into TiO₂ using the stepwise deposition-precipitation method (Neatu, Maciá-Agulló, Concepción, and Garcia, 2014). The results showed that the addition of Au to TiO₂ improved its visible light absorption efficiency, while the inclusion of Cu aided in the fixing of CO molecules on the catalyst surface, resulting in the direct reduction of CO to CH₄ under simulated sunlight. The catalyst containing Au-Cu/TiO₂ exhibited the highest formation rate of CH₄, reaching approximately 2200 μmolg⁻¹h⁻¹, whereas Au/TiO₂ and Cu/TiO₂ provided formation rates of approximately 210 and 280 μmolg⁻¹h⁻¹, respectively. FT-IR spectroscopy identified the presence of CO₂^{*} and Cu-CO bonds on the catalyst surface, indicating that the adsorption of CO on the catalyst surface was an important step before further reduction to CH₄ could occur. These observations corresponded to Cu-based catalysts. Peng et al. (2017) demonstrated that the selectivity of ethylene production was contingent on the adsorption energy of HCOOH or CO species on Cu surfaces. The researchers suggested that a key intermediate in the CO₂RR pathway to hydrocarbons involved the adsorption of CO molecules on the Cu surface with an optimal binding strength—neither too strong nor too weak. This allowed the CO molecules to be further hydrogenated into hydrocarbon species (e.g., C₂H₄) and desorbed from the surface. These observations are in line with the work of Zheng et al. (2019), which showed that the suitable adsorption energy of CO molecules on Cu-based catalysts plays a crucial role in converting CO₂ to C₂₊ products.

Based on the literature above, the CO₂ adsorption and intermediates binding energies on the catalyst surface can be considered a critical factor in initiating the subsequent reduction of CO₂ molecules. Numerous studies have reported that suitable binding energies contribute to the selectivity of the products formed. High binding energies suggest that the catalyst can firmly attach CO₂ and its intermediates to the catalyst surface. Following this, CO₂ and intermediates undergo further reduction, ultimately leading to the desorption of the desired products from the catalyst surface

(Chu et al., 2020; Jeong et al., 2020; Wang et al., 2020; Yang et al., 2020; Yin et al., 2020; Zheng et al., 2019).

Additionally, several studies have reported that introducing thermal energy can enhance the catalytic activity of CO₂RR. The presence of thermal energy facilitates the separation of photoinduced electron-hole pairs, thereby increasing the availability of charge carriers. This, in turn, leads to the generation of more photoinduced vacancies, which play a crucial role in the photothermal chemical cycle (Xu et al., 2018). In the context of photothermal catalysis for CO₂RR, the competition between desorption and reduction of key intermediates, such as CO*, HCOOH*, HCHO*, and CH₃OH*, significantly influences selectivity (Li et al., 2021). Upon completion of the reaction, the products are easily released, allowing the selected products to be obtained and reactant molecules to diffuse onto the catalyst surface. Consequently, the CO₂ reduction reaction proceeds efficiently.

In order to investigate the photoreduction of CO₂ on TiO₂-based catalysts in this research, rutile was chosen as the primary focus, owing to its superior reducing capability compared to anatase. Moreover, rutile has been reported to exhibit strong CO₂ binding energy, which further enhances CO₂RR (Kovačič et al., 2022). Rutile was grown on FTO substrates, and the reaction was conducted in the gas phase. Additionally, thermal energy was introduced into the catalytic system to examine its influence on the reactions. The study specifically explored the effects of the TiO₂ phase (e.g., rutile and anatase) and temperature on the photoreduction of CO₂. Analyzing these factors should provide valuable insights into optimizing TiO₂-based catalysts for CO₂RR application.

CHAPTER III

EXPERIMENTAL

3.1 Chemicals

The chemicals utilized in this study are listed in Table 3.1.

Table 3.1 Chemicals used in this research.

Chemicals	Formula	Content (%)	Suppliers
Acetone	CH ₃ COCH ₃	99.8	ACI Labscan
Ammonium hexafluoro titanate	(NH ₄) ₂ TiF ₆	99.99	Sigma-Aldrich
Ethanol	C ₂ H ₅ OH	99.7	ACI Labscan
Hydrochloric acid	HCl	37	Merck
Sodium hydroxide	NaOH	>97.0	Merck
Titanium n-butoxide	Ti(OCH ₂ CH ₂ CH ₂ CH ₃) ₄	97	Sigma-Aldrich
Argon	Ar	99.999	Linde
Mix gas:		99.999	
- Carbon monoxide	CO	5.11	
- Carbon dioxide	CO ₂	69.85	Linde
- Ethylene	C ₂ H ₄	4.92	
- Ethane	C ₂ H ₆	4.91	
- Methane	CH ₄	4.91	
Carbon dioxide	CO ₂	99.999	Si-Technology

3.2 Preparation of clean FTO substrate

Fluorine-doped tin oxide substrates (FTO, OPV Tech, 7-8 Ω /sq) were cut into a 2.5 x 6.0 cm² size. The FTO substrates were cleaned sequentially, involving washing with detergent, acetone, ethanol, and deionized (DI) water, with each step involving 15 minutes of ultrasonication. The cleaned substrates were stored in DI water until further use. Before use, the substrates were rinsed with DI water and air-dried.

3.3 Preparation of TiO₂ on FTO substrate

TiO₂ was directly grown on FTO substrates using a hydrothermal method reported in the literature (Butburee et al., 2019). Initially, a mixture of the desired amount of DI water and 37% HCl was prepared in polypropylene bottles under mechanical stirring. Subsequently, ammonium hexafluorotitanate (AFT) was added to the solution. Once a clear solution was obtained, a specific volume of titanium (IV) n-butoxide (TTBT) was added. Then, 35 mL of the mixed solution was transferred into a 50 mL Teflon-lined autoclave containing an FTO substrate, with its conductive side facing against the autoclave wall. The autoclave was secured with stainless steel and heated to 150 °C for an appropriate time. After that, the autoclave was let cool to room temperature, the TiO₂-coated electrode was removed and rinsed with DI water for 3 minutes. Before use, the electrodes coated with anatase TiO₂ were calcined at 600 °C for 2 hours to remove F atoms from the surface. No calcination was carried out on the electrodes coated with rutile TiO₂. Reactant contents and reaction time are shown in Table 3.2.

Table 3.2 The synthesis conditions for preparing TiO₂ on FTO substrate.

Samples	DI water (mL)	HCl (mL)	AFT (mg)	TTBT (mL)	Temperature (°C)	Time (h)	Calcine
{101}-{001}-1	40.0	20.0	400	1.0	150	24	yes
{101}-{001}-2	37.5	22.5	400	1.0	150	24	yes
{101}-{001}-3	35.0	25.0	400	1.0	150	24	yes
{010}-{001}-1	40.0	20.0	600	1.0	150	5	yes
{010}-{001}-2	37.5	22.5	600	1.0	150	5	yes
{010}-{001}-3	35.0	25.0	600	1.0	150	5	yes
Rutile	40.0	20.0	400	1.0	150	24	no

3.4 Characterization of catalysts

The crystal structures of TiO₂ were characterized using X-ray diffraction (XRD) performed on a Bruker D8 Advanced X-ray diffractometer, employing Cu K α irradiation at 40 kV and 40 mA with a diffracted beam monochromator.

UV-vis absorption spectra were obtained using a UV-Vis-NIR spectrophotometer (Shimadzu UV3600plus). Air was used as a background.

The percentages of each facet of TiO₂ were calculated from Raman spectra, which were acquired using a high-resolution Raman spectrometer (NTEGRA Spectra).

Morphology of the catalysts was obtained using Field-emission scanning electron microscopy (FESEM) (Hitachi SU8230) conducted at 10 keV.

The charge resistance of the electrodes was measured by electrochemical impedance spectroscopy (EIS) over a frequency range of 0.1 Hz to 100 kHz with a 10 mV amplitude.

Surface charge density (i.e., hole accumulation on the electrode surface) was evaluated using voltage-dependent conductive atomic force microscopy (CAFM) coupled with force-distance spectroscopy mapping (Bruker JPK Nanoscience), using a Pt tip (Bruker SCM-PIT-V2).

3.5 Incident photon to charge carrier efficiency of catalysts

The external quantum efficiency (EQE) of the photoanodes was measured using a Newport Oriel QEPVSI-b system under 300 W irradiation from a Xenon lamp equipped with a monochromator. Three electrodes were connected to a sample, and a 0.4 V RHE bias voltage was applied using a source meter (Keithley 2450). The excitation wavelength was swept from 200 to 1100 nm with an exposure mask of 0.04 cm².

3.6 Intensity-modulated photocurrent spectroscopy of samples

To investigate the charge transport properties of each sample, intensity-modulated photocurrent spectroscopy (IMPS) was conducted. IMPS measurements for samples with various facet pairs were carried out directly in 1 M NaOH solution using a three-electrode system (the same configuration as employed in PEC water splitting measurements) to simulate the actual environment of the water splitting process. A bias of 1.3 V vs Ag/AgCl was applied in each measurement using a Metrohm Autolab PGSTAT302N potentiostat. An Autolab LED driver was utilized to power a triple light-emitting diode (LED) array (LDC470-blue, $\lambda = 470$ nm) as a light source with an intensity of 80 mW/cm², providing both AC and DC components of the illumination in frequency response analyzer mode with a frequency range of 4000–100 Hz. Data was collected

using NOVA 2.1.4 software. The mean transit time (τ_{tr}) is employed to indicate charge carrier kinetics. τ_{tr} can be calculated from equation (3.1).

$$\tau_{tr} = \frac{1}{2\pi f_{min}} \quad (3.1)$$

Where f_{min} is the characteristic frequency minimum of the IMPS imaginary component (Yu et al., 2013).

3.7 PEC water splitting performance measurements

The PEC water splitting performance was assessed using a photo-reactor with a three-electrode system. The prepared TiO₂-coated electrode, Ag/AgCl electrode, and Pt electrode served as the working, reference, and counter electrode, respectively. The reaction was conducted in a 1 M NaOH solution. The solution was purged with Ar gas for 30 minutes before initiating the reaction. The current density was measured using an electrochemical workstation (AMATEX PMC-CH508A) under simulated solar light irradiation (LCS-100 solar simulator) at 1 sun of light intensity (AM 1.5 G filter, 1 kW/m²). Linear sweep voltammetry (LSV) was performed with a scan rate of 10 mV/s. The potential versus RHE was converted using equations (3.2) and (3.3), where NHE represents the normal hydrogen electrode.

$$E(\text{vs RHE}) = E(\text{vs Ag/AgCl}) + E_{\text{Ag/AgCl}}(\text{Reference}) + 0.059 \times \text{pH} \quad (3.2)$$

where

$$E_{\text{Ag/AgCl}}(\text{Reference}) = 0.1976 \text{ V vs NHE at } 25^\circ \text{C} \quad (3.3)$$

The reaction was performed under the same procedures for 6 h for the stability test.

3.8 Photo CO₂RR catalytic performance measurements

Photo-catalytic CO₂RR was performed in a homemade gas phase reactor. The electrode with a 3.0 x 3.0 cm² dimension was placed in the reactor chamber. CO₂ was bubbled through DI water for 15 min to feed CO₂ with vaporized water into the reactor. UV light at 370 nm (LED PR160L-370nm) was used as a light source. The reaction temperature at 25, 40, 60, and 80 °C was controlled by a water bath. The reaction was carried on for 6 h before the product analysis by a gas chromatograph (SHIMADZU, Nexis, GC-2030).

CHAPTER IV

RESULTS AND DISCUSSION

4.1 PEC water splitting by anatase TiO₂

4.1.1 Synthesis of anatase TiO₂ films

The critical elements governing the formation of low-index facets in TiO₂, as reported in the literature (Butburee et al., 2019), have facilitated a comprehensive alignment of low-index facets in this study. A simple hydrothermal synthesis using tetrabutyl titanate (TTBT) as a Ti⁴⁺ source, ammonium hexafluorotitanate (AFT) as a fluoride (F⁻) source, and hydrochloric acid (HCl) as an H⁺ source was utilized to successfully grow TiO₂ crystals with tuned facets on a fluorine-doped tin oxide (FTO) substrate. Parameters, specifically the amount of H⁺ and F⁻, were carefully adjusted to achieve {101}-{001} and {010}-{001} pairs with varying facet ratios.

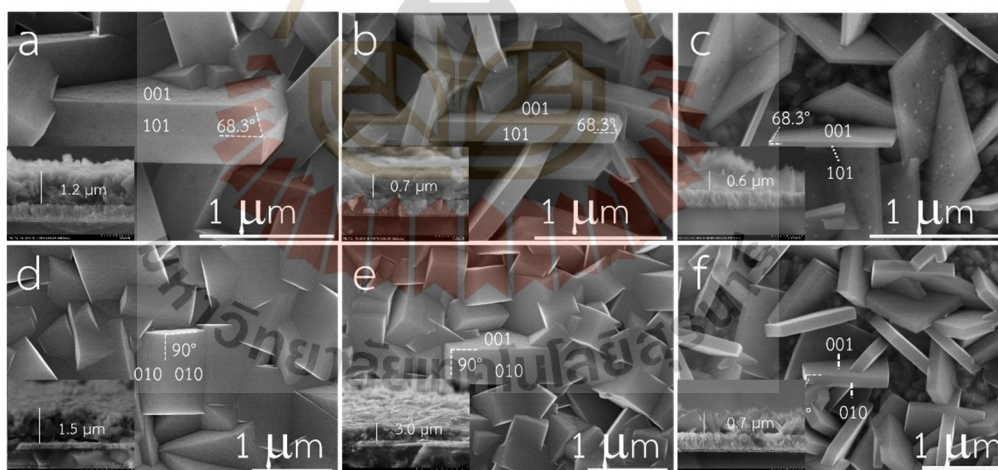


Figure 4.1 SEM images showing the morphology of single-crystalline anatase TiO₂, a-c) {101}-{001} facets with different {101}/ {001} facet ratios and d-e) {010}-{001} facets with different {010}/ {001} facet ratios. Reprinted (adapted) with permission from (Phawa et al., 2021). Copyright 2021 ChemCatChem.

Figure 4.1 confirms that single-crystalline TiO_2 crystals were successfully grown on the FTO substrate. As displayed in Figure 4.1a-c, scanning electron microscope (SEM) images show that trapezoidal $\{101\}$ and square $\{001\}$ facets emerge at relatively low F concentration (400 mg of AFT). The angle between $\{101\}$ and $\{001\}$ facets equals 68.3° , which is consistent with Barnard and Curtiss's predictions (Barnard and Curtiss, 2005). The crystal thickness could be further adjusted by modifying the HCl concentration. Figures 4.1a-c show samples of crystal $\{101\}$ - $\{001\}$ facet pairs. Thicker crystals, denoted as $\{101\}$ - $\{001\}$ -1, appeared at a lower HCl amount (HCl=20.0 mL), as shown in Figure 4.1a. In Figures 4.1b and 4.1c, crystals became thinner when the HCl amount was increased to 22.5 and 25.0 mL, respectively. This occurs because the rise in H^+ concentration lowers the surface energy of the $\{001\}$ facet compared to the $\{101\}$ facet, limiting crystal growth along the $\{001\}$ direction and resulting in a larger percentage of the $\{001\}$ facet (Butburee et al., 2019; Shiu et al., 2012). The samples generated from these synthesis conditions are designated as $\{101\}$ - $\{001\}$ -2 and $\{101\}$ - $\{001\}$ -3, respectively. The film thickness also corresponds to the crystal thickness, as shown in the inset images.

Particles composed of rectangular $\{010\}$ and square $\{001\}$ facets with a 90° interfacial angle were formed when the F^- amount in the system was increased (AFT raised from 400 mg to 600 mg), as seen in SEM images (Figure 4.1d-f). Similar to the $\{101\}$ - $\{001\}$ pair case, the thickness of crystals formed by $\{010\}$ and $\{001\}$ facets could also be adjusted by varying the H^+ amount from 20.0 mL to 22.5 and 25 mL, respectively. The samples obtained from these conditions, as shown in Figure 4.1d-f, are labeled as $\{010\}$ - $\{001\}$ -1, $\{010\}$ - $\{001\}$ -2, and $\{010\}$ - $\{001\}$ -3, respectively.

X-ray diffraction (XRD) patterns of $\{101\}$ - $\{001\}$ (Figure 4.2a) and $\{010\}$ - $\{001\}$ (Figure 4.2b) films display characteristic anatase peaks (101), (200), (211), and (204) at $2\theta=25.3, 48.0, 55.0,$ and 62.6 (PDF-01-070-8505), respectively. In both facet pairs, the characteristic peak intensity of the FTO substrate is in opposition to the crystal thickness. The substrate diffraction is more guarded by thicker crystal and film, resulting in lower relative intensity of characteristic substrate peaks.

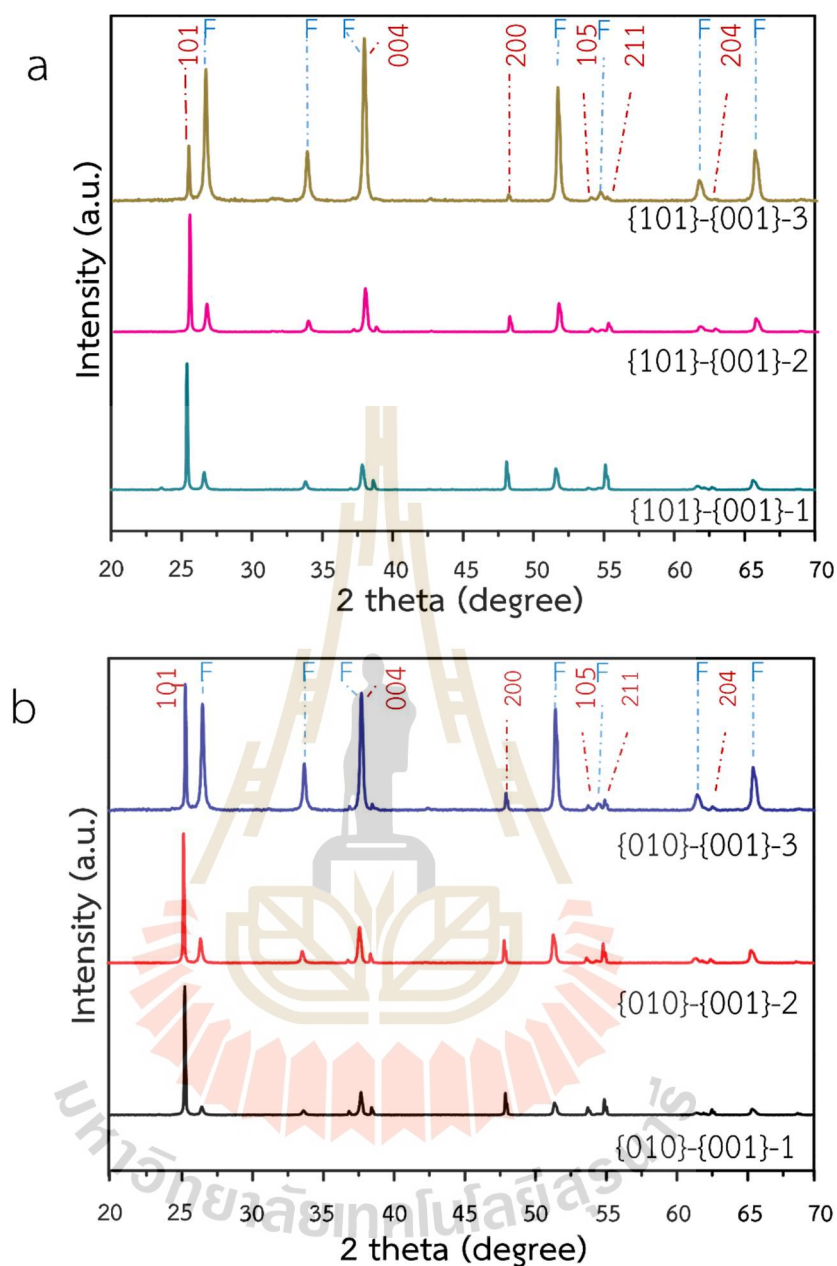


Figure 4.2 XRD patterns of anatase TiO_2 with a) $\{101\}$ - $\{001\}$ and b) $\{010\}$ - $\{001\}$ facet pairs. Reprinted (adapted) with permission from (Phawa et al., 2021). Copyright 2021 ChemCatChem.

Typically, the facet ratio of TiO_2 crystal can be roughly calculated from XRD patterns, but this technique is difficult to determine the facet ratios of thin films accurately. As a result, Raman spectroscopy, a more accurate method for quantifying the percentage of $\{001\}$ in TiO_2 crystals, was employed (Tian, Zhang, Zhang, and Pan, 2012). Distinct Raman spectra of TiO_2 are known to originate from various vibrational

modes of O-Ti-O (Roy, Park, Sohn, Leung, and Pradhan, 2014; Tian et al., 2012). The A_{1g} peak in Raman spectra represents the antisymmetric bending vibration of O-Ti-O, which appears in the {001} facet. In contrast, the E_g peak indicates symmetric stretching vibration of O-Ti-O in non-exposed {001} facets. Based on the method proposed by Tian et al. (2012), the percentages of the {001} facet can be calculated from the ratio between A_{1g} and E_g intensities. Figure 4.3a and 4.3b display Raman spectra of samples comprising {101}-{001} and {010}-{001} facet pairs, respectively. To estimate {001} facet percentage, the below equation can be applied.

$$\% \{001\} = \frac{\text{Intensity of } A_{1g}}{\text{Intensity of } E_g} \times 100 \quad (4.1)$$

The calculated facet percentages are summarized in Table 4.1. As expected, the {001} percentage increases as particle thickness decreases. For instance, {101}-{001}-1 with the thickest particles has 38% {001}, while {101}-{001}-2 and {101}-{001}-3 have 47% and ~100%, respectively. A similar trend is also observed for the {010}-{001} pair. Additionally, atomic force microscopy (AFM) was employed to estimate the surface area of the electrode. The topology images of synthesized samples in Figure 4.4 also indicate the roughness of the films. The decrease in crystal thickness results in rougher film. The estimated surface areas of the samples are presented in Table 4.1.

Table 4.1 The band gap energy, surface area per cm^2 , and facet percentages of crystal samples.

Samples	Band gap energy (eV)	Surface area per cm^2 (cm^2)	{001} (%)	{101} (%)	{010} (%)
{101}-{001}-1	3.37	1.93	38	62	-
{101}-{001}-2	3.39	2.23	47	53	-
{101}-{001}-3	3.55	1.88	~100	0	-
{010}-{001}-1	3.35	1.89	39	-	61
{010}-{001}-2	3.40	1.51	57	-	43
{010}-{001}-3	3.42	1.94	67	-	33

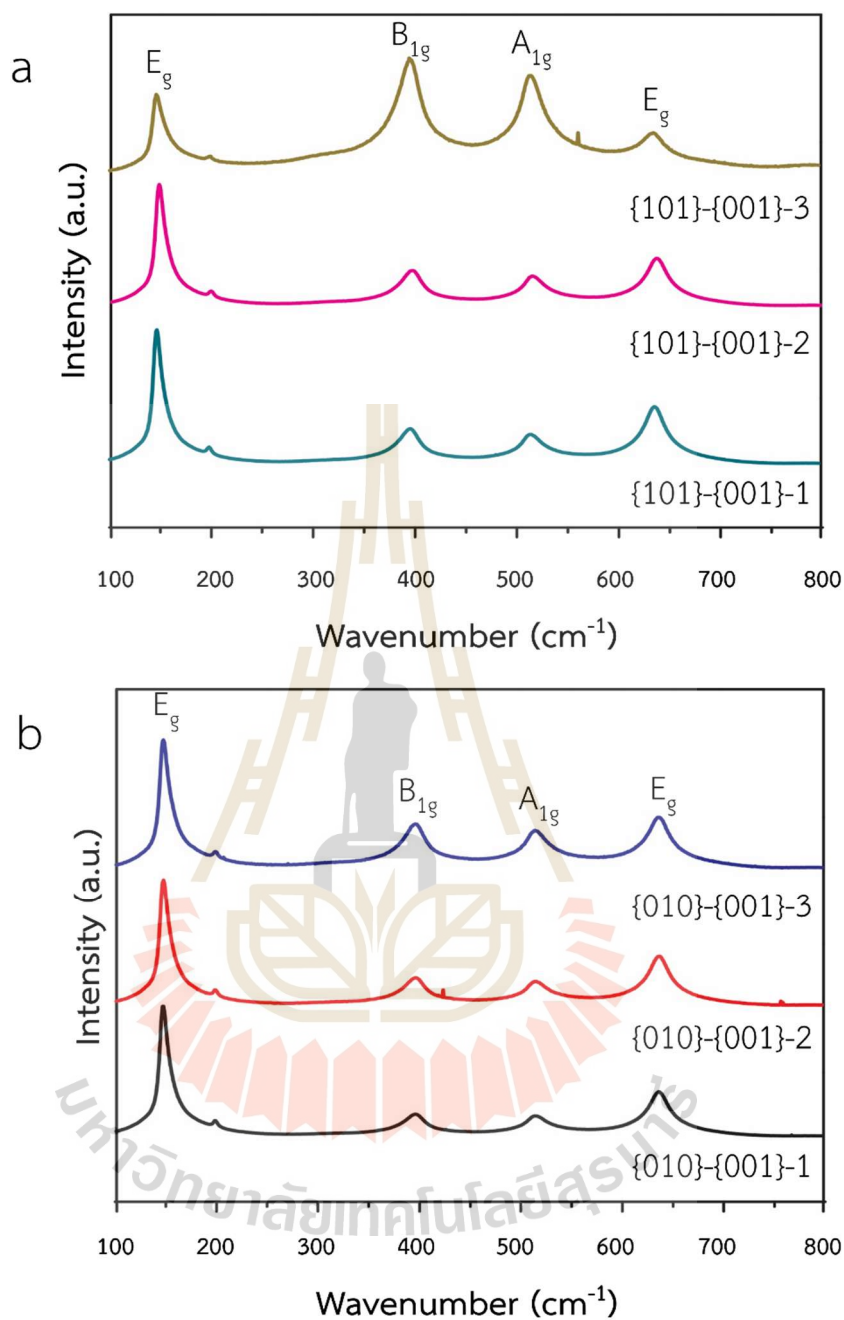


Figure 4.3 Raman spectra of anatase TiO_2 with a) $\{101\}$ - $\{001\}$ and b) $\{010\}$ - $\{001\}$ facet pairs. Reprinted (adapted) with permission from (Phawa et al., 2021). Copyright 2021 ChemCatChem.

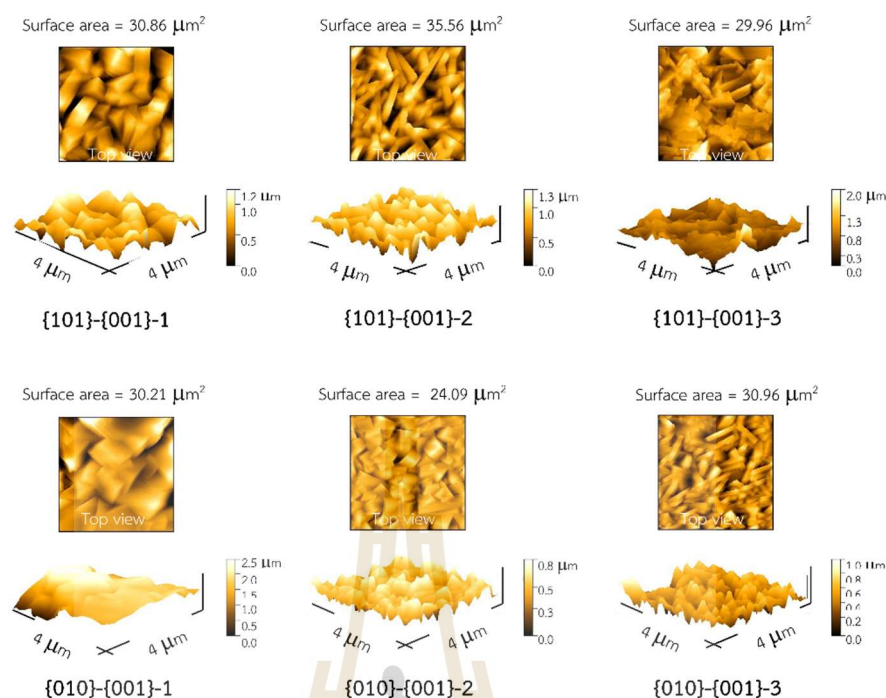


Figure 4.4 Surface area estimation of $16 \mu\text{m}^2$ scanned area based on AFM. Reprinted (adapted) with permission from (Phawa et al., 2021). Copyright 2021 ChemCatChem.

UV-visible absorption spectra of TiO_2 films with facet pairs are shown in Figure 4.5. The absorbance decreases with a reduction in the thickness and density of crystals with $\{101\}$ - $\{001\}$ facet pair, as shown in Figure 4.5a. Meanwhile, the absorbance of the $\{010\}$ - $\{001\}$ facet pair exhibits less variation, as the density of the crystals does not differ significantly. These observations are in good agreement with the SEM results. A noticeable blue shift is evident when the crystals become thinner in both $\{101\}$ - $\{001\}$ and $\{010\}$ - $\{001\}$ pairs. For instance, the samples with the thickest crystals in both facet pairs ($\{101\}$ - $\{001\}$ -1 and $\{010\}$ - $\{001\}$ -1) display light absorption edges of approximately 377 nm, while those with the thinnest crystals in both facet pairs ($\{101\}$ - $\{001\}$ -3 and $\{010\}$ - $\{001\}$ -3) exhibit significant blue-shifts to around 340 nm and 364 nm, respectively. This observation is consistent with previous studies, which showed that the blue shift becomes more noticeable as the amount of high-energy $\{001\}$ facet increases, potentially due to the shifted conduction band minimum of the $\{001\}$ facet (Butburee et al., 2019; Liu et al., 2010; Ye, Mao, et al., 2013).

Figure 4.6 displays the Tauc plots constructed using the Kubelka-Munk method. The Tauc plots were extrapolated to determine the bandgap energy. The corresponding bandgaps correlate with the blue shift observed in Figure 4.5.

Furthermore, the {001} facet percentage is also consistent with the bandgap energy, which increases in correspondence with the shifted conduction band minimum. The estimated band gap energies are shown in Table 4.1.

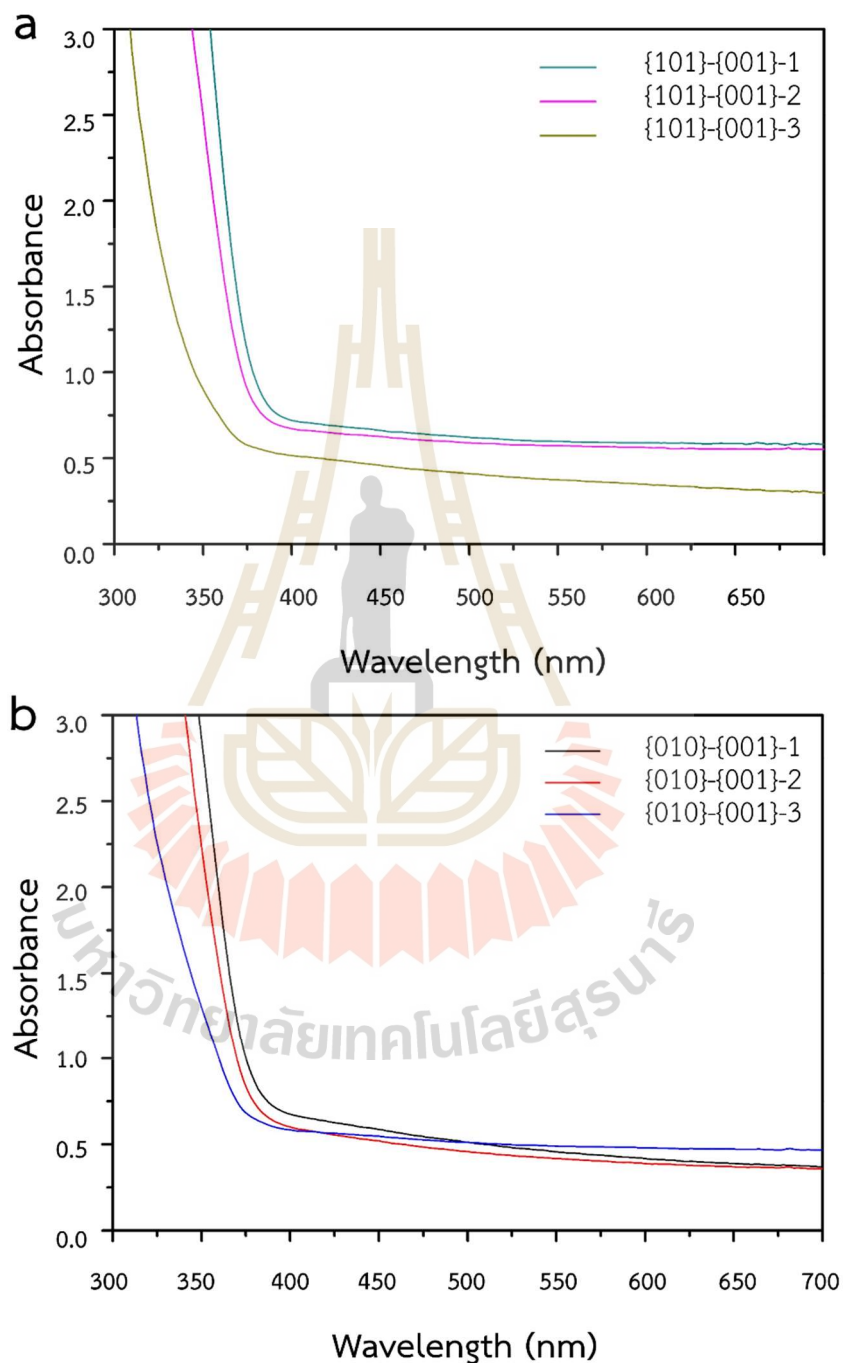


Figure 4.5 UV-Vis absorption spectra of anatase TiO₂ with a) {101}-{001} and b) {010}-{001} facet pairs. Reprinted (adapted) with permission from (Phawa et al., 2021). Copyright 2021 ChemCatChem.

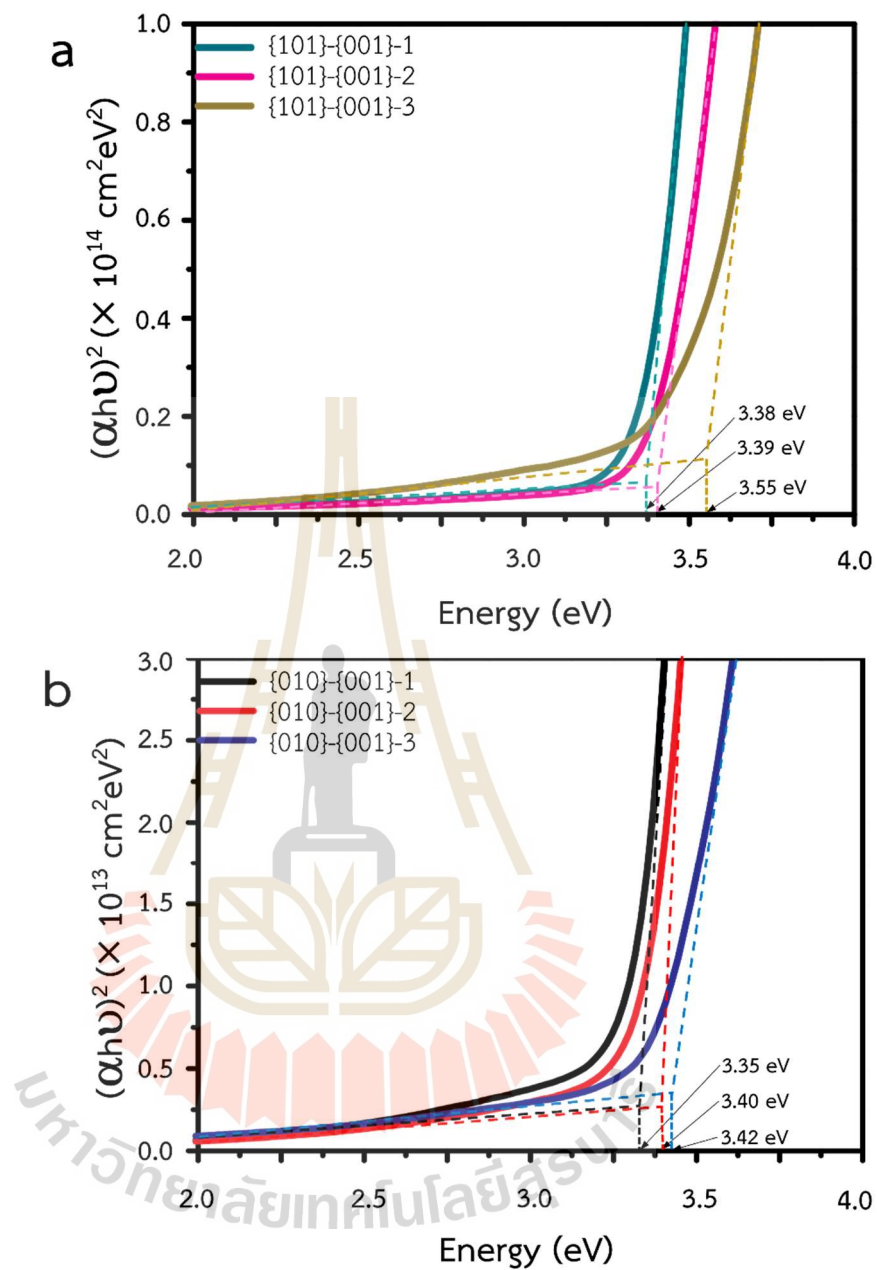


Figure 4.6 Tauc plots of anatase TiO_2 with a) {101}-{001} and b) {010}-{001} facet pairs. Reprinted (adapted) with permission from (Phawa et al., 2021). Copyright 2021 ChemCatChem.

4.1.2 PEC water splitting activities

The PEC water splitting performance of the samples appears to depend more on the type of facet pairs rather than the band gap or surface area. For example, in the case of {101}-{001}, PEC water splitting performance seems to increase with a higher {001} ratio. As observed in Figure 4.7a, the current-voltage (i-v) curve with chopped light for the sample with the {101}-{001} pair at different {001}/{101} facet ratios, {101}-{001}-3 with the highest percentage of {001} facet exhibits the highest photocurrent, even though it has the widest band gap (3.55 eV) and lowest surface area (1.88 cm²) among the samples in the same set. At the water splitting potential (1.23 V vs. RHE), {101}-{001}-3 demonstrates a photocurrent of 0.24 mA/cm², while {101}-{001}-2 and {101}-{001}-1 show 0.22 mA/cm² and 0.15 mA/cm², respectively.

On the other hand, unexpected results were observed for the {010}-{001} facet pairs. The sample with the highest {001} percentage ({010}-{001}-3) does not exhibit the best PEC water splitting performance. As shown in Figure 4.7b, the photocurrent generated by {010}-{001}-3 is surpassed by that of {010}-{001}-1, which has the lowest percentage of {001} (0.24 mA/cm² at 1.23 V vs RHE). Furthermore, PEC water splitting performance for this set of samples ({010}-{001} facet pair) does not display a clear trend. For instance, {010}-{001}-2, which has a moderate {001} facet ratio compared to {010}-{001}-1 and {010}-{001}-3, demonstrates the worst PEC water splitting performance.

The corresponding incident photon to charge carrier efficiency (IPCE) of all samples is shown in Figure 4.7. The maximum IPCE values (at $\lambda=314$ nm) for {101}-{001}-1, {101}-{001}-2, and {101}-{001}-3 are 53.5%, 59.6%, and 82.0%, while those for {010}-{001}-1, {010}-{001}-2, and {010}-{001}-3 are 81.6%, 66.9%, and 76.0%, respectively. The IPCE results are in good agreement with the PEC water splitting performance of the samples. Additionally, the samples display excellent stability, with only a slight drop in photocurrent observed after six hours of illumination, as shown in Figure 4.9.

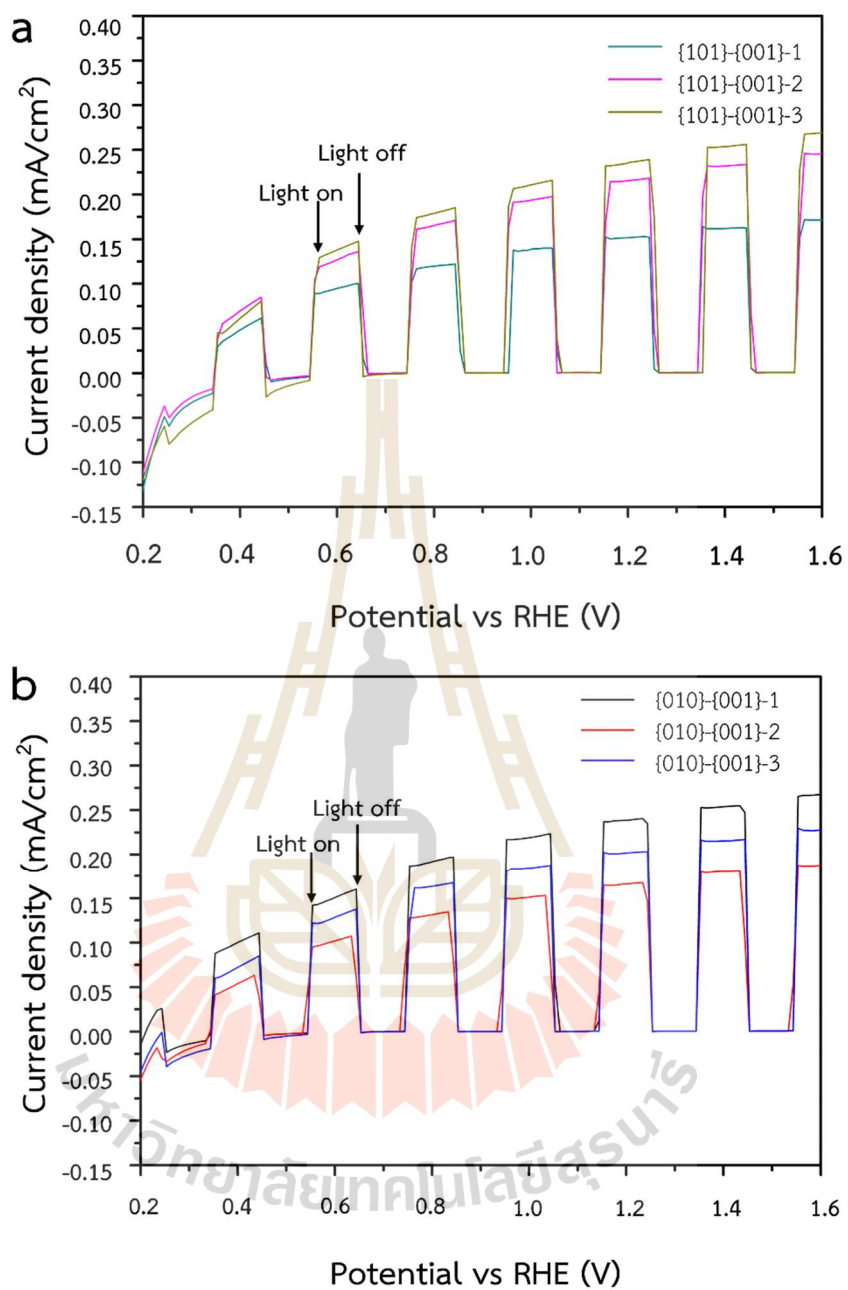


Figure 4.7 The PEC water splitting performance of anatase TiO₂ with a) {101}-{001} and b) {010}-{001} facet pairs. Reprinted (adapted) with permission from (Phawa et al., 2021). Copyright 2021 ChemCatChem.

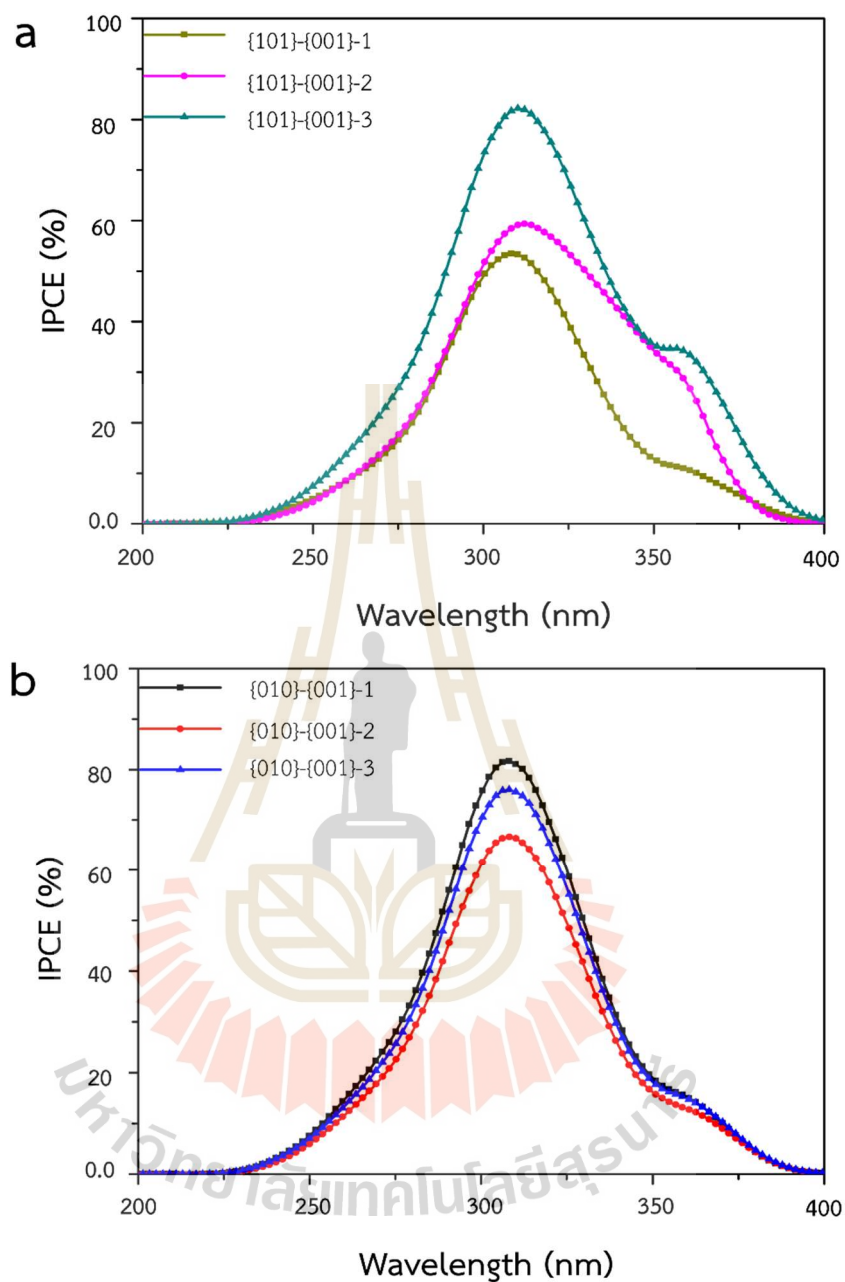


Figure 4.8 IPCE of anatase TiO_2 with a) $\{101\}$ - $\{001\}$ and b) $\{010\}$ - $\{001\}$ facet pairs. Reprinted (adapted) with permission from (Phawa et al., 2021). Copyright 2021 ChemCatChem.

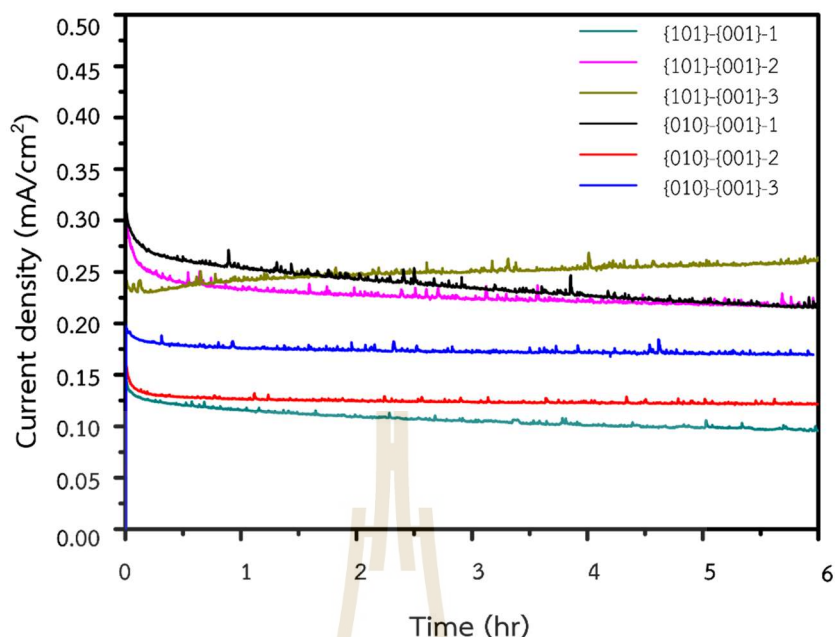


Figure 4.9 Photocurrents generated by various samples tested under the simulated sunlight (AM 1.5) for 6 hr at the applied voltage of 0.6 V vs Ag/AgCl. Reprinted (adapted) with permission from (Phawa et al., 2021). Copyright 2021 ChemCatChem.

The synergistic effects of various factors should be considered to understand the complicated trends of PEC water splitting performance in these faceted TiO₂ electrodes. Electrochemical impedance spectroscopy (EIS) measurement was performed to elucidate charge transfer kinetics in the nanostructured electrodes. Figures 4.10a and 4.10b present the Nyquist plot of {101}-{001} and {010}-{001} sample sets, which are fitted with an equivalent circuit (inset), respectively. All samples exhibit the same Nyquist plot feature, consisting of a high-frequency intercept on the real axis (Z') representing the series resistance (R_S), and a semicircle in a high-to-medium frequency region representing a combination of constant phase element (Q) and charge transfer resistance (R_{CT}) (Butburee et al., 2018; Wang et al., 2016; Xia, Wang, Lin, and Lu, 2012). The similar Z' suggests that all samples have comparable R_S , meaning that the intrinsic resistance of the material, the contact resistance (between the material films and the current collectors), and the ionic resistance of the electrolyte are similar (Xu, Kong, Zhou, and Li, 2007). This result is expected because all films are made of the same material, grown on the same substrate, and tested under identical conditions.

The semicircles in the high-to-medium frequency region are significantly different. As shown in Figure 4.10a, among the set of {101}-{001} samples, {101}-{001}-1 exhibits the largest semicircle, indicating its high charge transfer resistance, while {101}-{001}-2 and {101}-{001}-3 show similar-sized semicircles, significantly smaller than that of {101}-{001}-1, suggesting more efficient charge transport kinetics (Xia et al., 2012). It is noticeable from this set of samples that, in the {101}-{001} pair, a higher percentage of {001} corresponds to higher charge transport efficiency. In contrast, in the case of the {010}-{001} pair, the sample with a lower percentage of {001} (sample {101}-{001}-1) demonstrates better charge transport than the sample with a higher percentage of {001}, as shown in Figure 4.10b.

Intensity-modulated photocurrent spectroscopy (IMPS), a transient photocurrent measurement technique to evaluate charge transport, was applied to gain insight into the kinetics of carrier extraction in the photoelectrodes (Barnes et al., 2013; Butburee et al., 2018). IMPS results in Figure 4.11 reveal that, generally, the mean transit times (τ_{tr}) of photogenerated electrons (e^-) for {101}-{001}-1, {101}-{001}-2, and {101}-{001}-3 are 0.28, 0.18, and 0.10 ms, respectively. The shorter τ_{tr} indicates more efficient electron transport from the material films to the FTO substrate, which acts as the current collector (Butburee et al., 2018; Mao et al., 2016). The superior charge transport efficiency of {101}-{001}-3 could contribute to the highest photocurrent density achieved among the same set of samples constructed by the {101}-{001} facet pair. τ_{tr} is also an excellent factor reflecting the performance of the samples with the {010}-{001} facet pair, as {010}-{001}-1, with the lowest τ_{tr} of 0.08 ms, has higher PEC performance than {010}-{001}-3 ($\tau_{tr} = 0.10$ ms) and {010}-{001}-2 ($\tau_{tr} = 0.15$ ms), respectively.

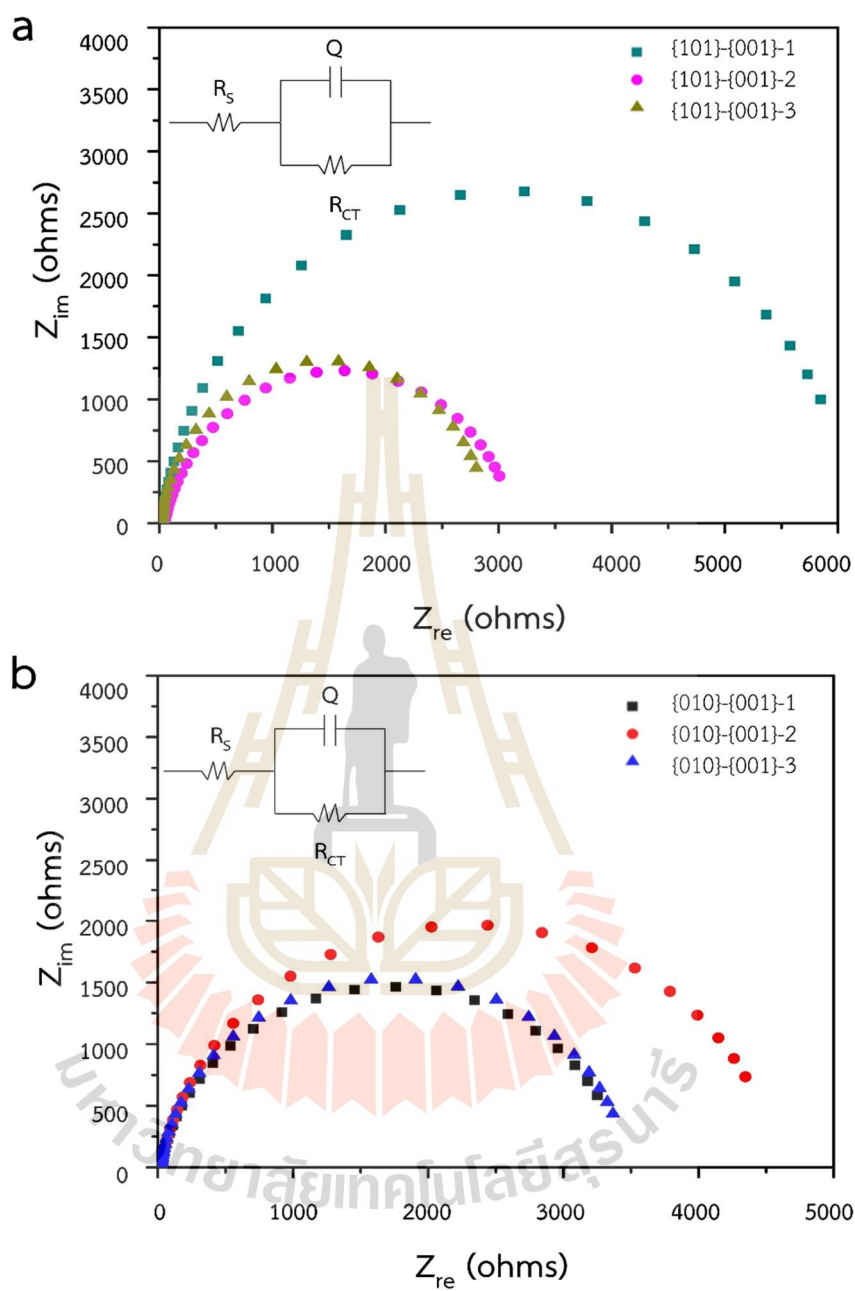


Figure 4.10 The EIS spectra of anatase TiO_2 with a) $\{101\}$ - $\{001\}$ and b) $\{010\}$ - $\{001\}$ facet pairs. Reprinted (adapted) with permission from (Phawa et al., 2021). Copyright 2021 ChemCatChem.

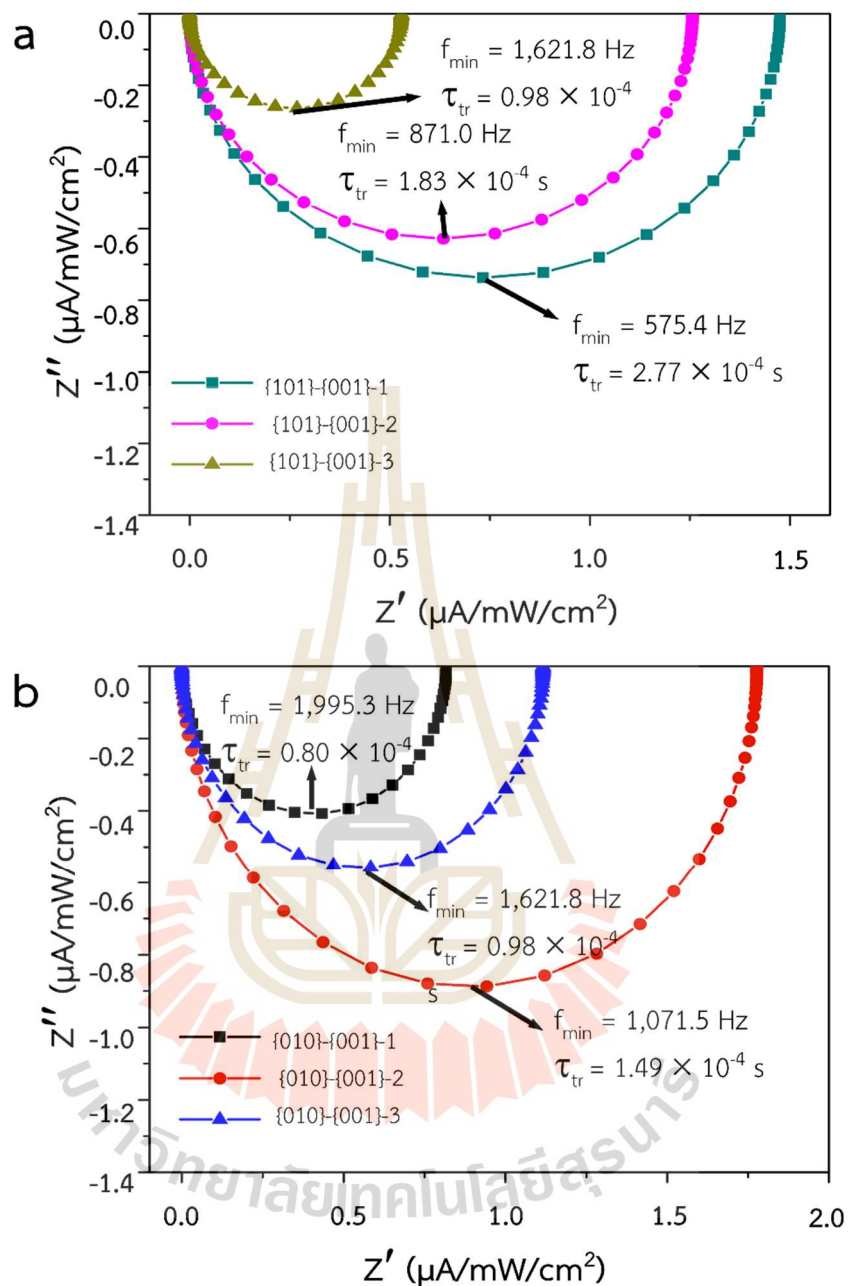


Figure 4.11 IMPS spectra of anatase TiO_2 with a) $\{101\}$ - $\{001\}$ and b) $\{010\}$ - $\{001\}$ facet pairs. Reprinted (adapted) with permission from (Phawa et al., 2021). Copyright 2021 ChemCatChem.

This phenomenon is in excellent agreement with the theoretical study on the electron affinity of different TiO_2 facets reported by Zhao and coworker (Zhao, Li, and Zou, 2010). Based on density functional theory (DFT) calculations, the group proposed that the electron affinity (χ), the ability to acquire electrons, follows the

order of $\{101\} > \{001\} > \{010\}$ (for the relaxed surfaces, $\chi_{\{101\}} = 4.384$, $\chi_{\{001\}} = 3.193$, $\chi_{\{010\}} = 2.807$ eV, respectively). Considering the total electron affinity, which is weighted by the percentages of the facets in the samples, the total electron affinities of $\{101\}$ - $\{001\}$ -1, $\{101\}$ - $\{001\}$ -2, and $\{101\}$ - $\{001\}$ -3 are 3.93, 3.82, and 3.19 eV, respectively. The calculation details are shown in Table 4.2. Since electron affinity is the ability to attract electrons, the film with a higher electron affinity value is more likely to accumulate electrons on itself. These accumulated electrons can recombine with holes (h^+), leading to fewer holes left for water oxidation. Consequently, $\{101\}$ - $\{001\}$ -1, which has the highest electron affinity value among the samples in this set, exhibits the lowest PEC performance, while $\{101\}$ - $\{001\}$ -2 and $\{101\}$ - $\{001\}$ -3, which have lower electron affinity values, show better PEC performance.

Similarly, the total electron affinities of $\{010\}$ - $\{001\}$ -1, $\{010\}$ - $\{001\}$ -2, and $\{010\}$ - $\{001\}$ -3 are 2.96, 3.03, and 3.07 eV, respectively. The $\{010\}$ - $\{001\}$ -1, which has a significantly lower electron affinity in this set of the same facet pair, exhibits the best PEC performance.

Table 4.2 Total electron affinity of anatase TiO₂.

Samples	Calculation method	Total electron affinity
$\{101\}$ - $\{001\}$ -1	$(\frac{62}{100})(4.384) + (\frac{38}{100})(3.193)$	3.93
$\{101\}$ - $\{001\}$ -2	$(\frac{53}{100})(4.384) + (\frac{47}{100})(3.193)$	3.82
$\{101\}$ - $\{001\}$ -3	$(\frac{0}{100})(4.384) + (\frac{100}{100})(3.193)$	3.19
$\{010\}$ - $\{001\}$ -1	$(\frac{61}{100})(2.807) + (\frac{39}{100})(3.193)$	2.96
$\{010\}$ - $\{001\}$ -2	$(\frac{43}{100})(2.807) + (\frac{57}{100})(3.193)$	3.03
$\{010\}$ - $\{001\}$ -3	$(\frac{33}{100})(2.807) + (\frac{67}{100})(3.193)$	3.07

On the other hand, it is noteworthy that the total electron affinity values of $\{010\}$ - $\{001\}$ -2 and $\{010\}$ - $\{001\}$ -3 are nearly the same, 3.03 and 3.07 eV, respectively. In this case, electron affinity cannot significantly affect water oxidation performance. The

other factor, dissociative adsorption ability of water molecules on the facets, should consequently play a role. It is well known that, among the low-index facets of anatase, the {001} facet is more favorable for dissociative adsorption of water molecules (Liu et al., 2014; Vittadini, Selloni, Rotzinger, and Grätzel, 1998), and hence facilitates the cleavage of water. As a consequence, {010}-{001}-3, which has a higher percentage of {001}, is likely to exhibit better water splitting behavior than {010}-{001}-2. This result correlates well with the PEC water splitting behavior (Figure 4.7). As a final remark, it is interesting to note that the electrostatic adhesion related to upward band bending – hole affinity – increases with an applied positive bias, as shown in Figure 4.12, corresponding to the voltage dependence of the reaction current density shown in Figure 4.7.



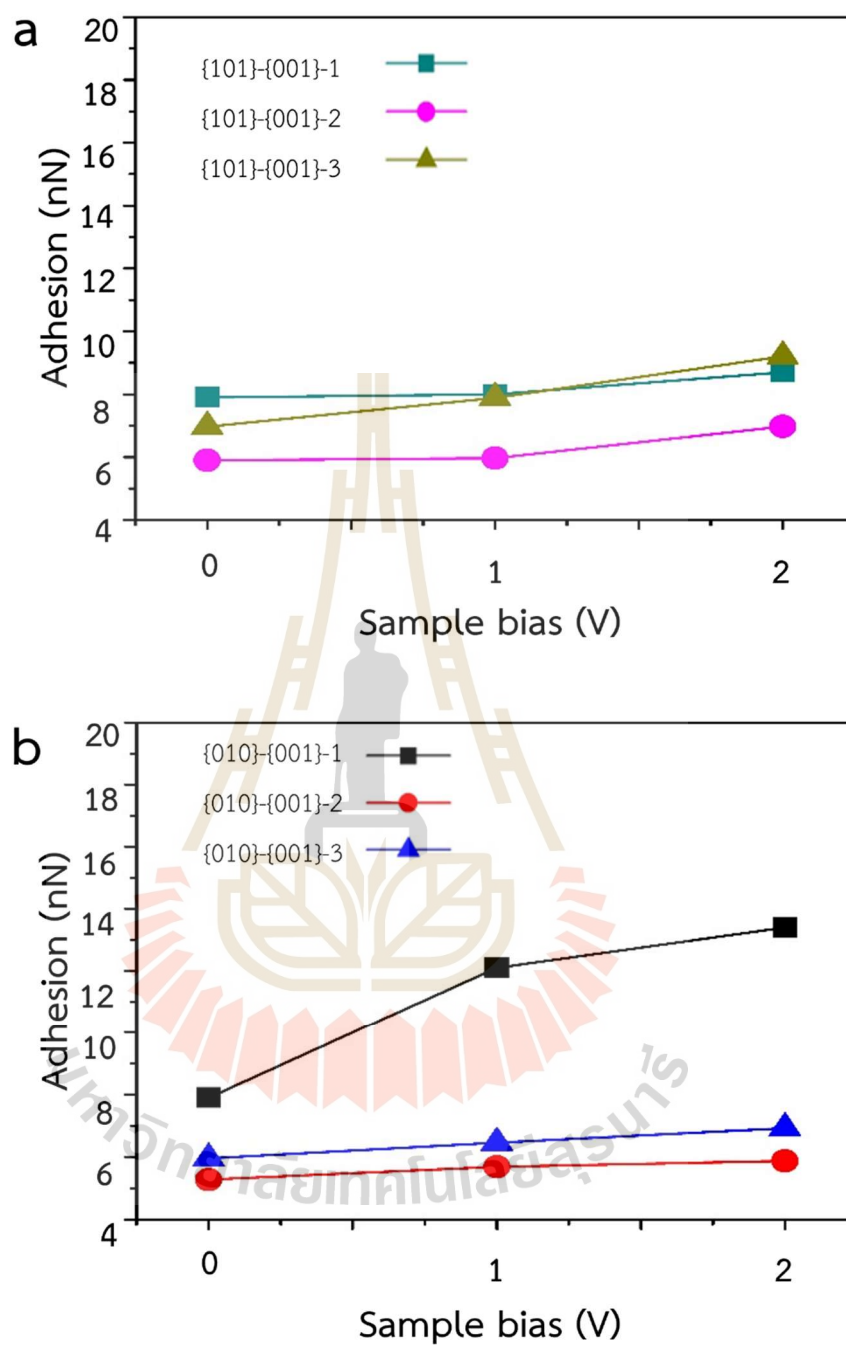


Figure 4.12 Adhesion force of anatase TiO₂ surface with a) {101}-{001} and b) {010}-{001} facet pairs. Reprinted (adapted) with permission from (Phawa et al., 2021). Copyright 2021 ChemCatChem.

4.2 CO₂ photo-thermal reduction reaction by rutile and anatase TiO₂

4.2.1 Synthesis of rutile and anatase TiO₂ films

From the previous study, anatase TiO₂ with the {101}-{001} facet pair was chosen because its ability to adsorb water molecules was less than the {010}-{001} facet pair, which could lead to a better possibility for CO₂ adsorption (Phawa et al., 2020). Rutile TiO₂ was prepared with similar procedures to the synthesis of anatase TiO₂, but ammonium hexafluoro titanate was not added. Both single-crystalline rutile and anatase TiO₂ were grown on FTO substrates to improve charge transport. SEM images in Figure 4.13 show rutile and anatase crystals of various sizes. Due to the absence of F⁻ ions, the surface energy of rutile is lower than anatase during the crystal growth process. After the reaction was done, rutile was accordingly obtained. In addition, F⁻ ions play a key role in phase transformation. F⁻ ions do not only control the facet pairs but also reduce the surface energy of anatase during the crystal growth process. Hence, with the addition of AFT, the surface energy of anatase is lower than rutile resulting in the presence of the anatase phase after the synthesis (Butburee et al., 2019).

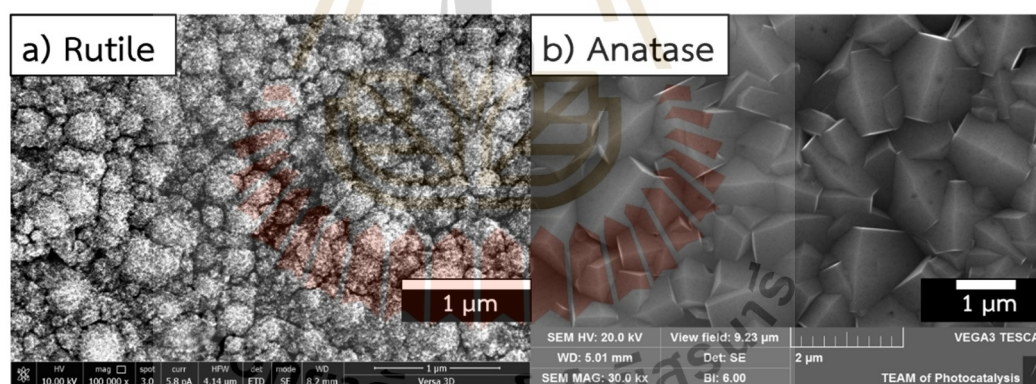


Figure 4.13 SEM images showing the morphology of single-crystalline of a) rutile and b) anatase TiO₂.

Figure 4.14 shows the XRD patterns of rutile and anatase phases of TiO₂, which correspond with SEM images. The peaks at $2\theta = 36.1^\circ$ and 62.9° represent the (101) and (002) planes, which indicate the characteristic features of rutile. The maximum peak intensity of rutile at 62.9° well indicates the nanorods oriented perpendicular to the FTO substrate, corresponding with the literature (Sadhu and Poddar, 2014). The characteristic peaks of anatase at $2\theta = 25.3^\circ$, 48.0° , 38.8° , and 55.0° represent the (101), (004), (200), and (105) planes, respectively.

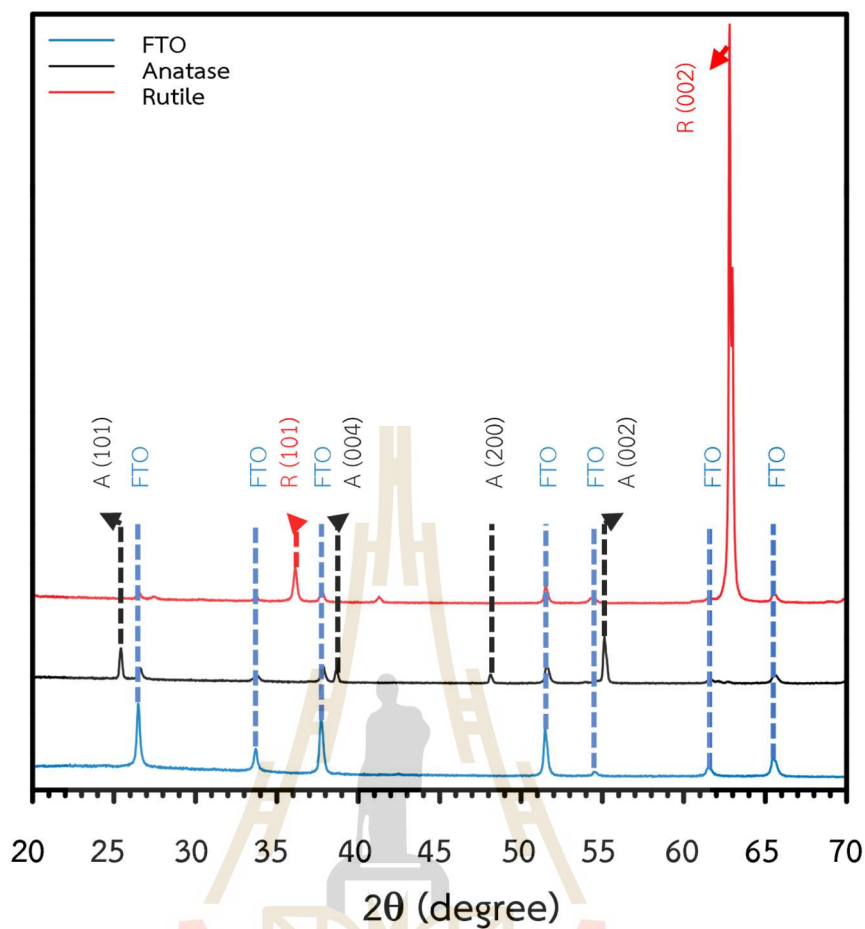


Figure 4.14 XRD patterns of synthesized rutile and anatase TiO_2 .

The diffuse reflectance spectra of the synthesized catalysts are shown in Figure 4.15. Both samples absorbed UV radiation and the absorption edges of the rutile and anatase TiO_2 were at 404 nm and 377 nm. The anatase TiO_2 's higher reflectance in the visible region could be from the thicker and denser crystals on the FTO substrate than the rutile TiO_2 , as observed in the SEM images. Furthermore, the Tauc plots in Figure 4.16, derived from the Kubelka-Munk function, show that the estimated band gap energies for rutile and anatase TiO_2 are 3.00 eV and 3.22 eV, respectively. These results are consistent with the characteristic electronic properties of rutile and anatase (Mi and Weng, 2015; Scanlon et al., 2013).

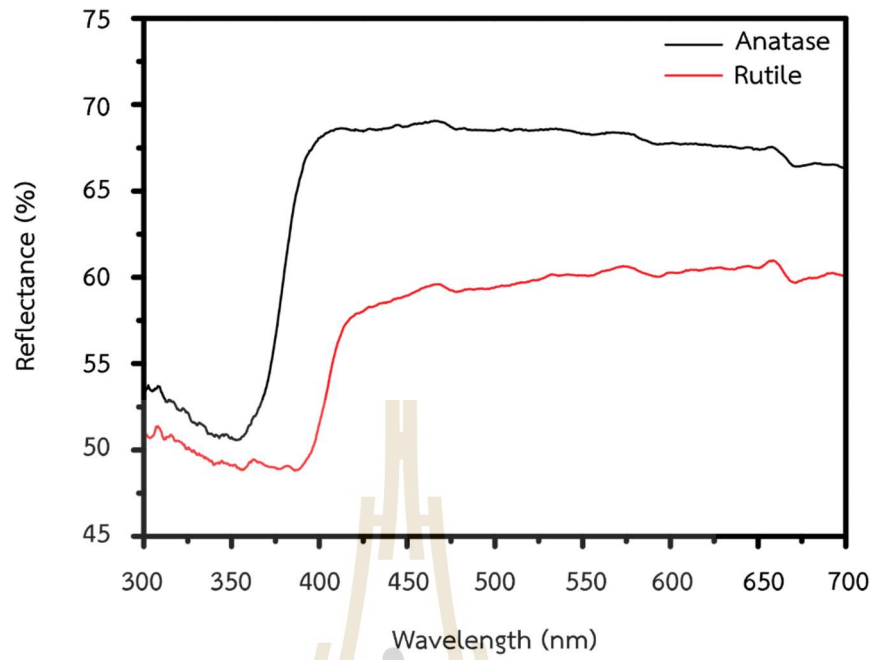


Figure 4.15 Diffuse reflectance spectra of rutile and anatase TiO_2 .

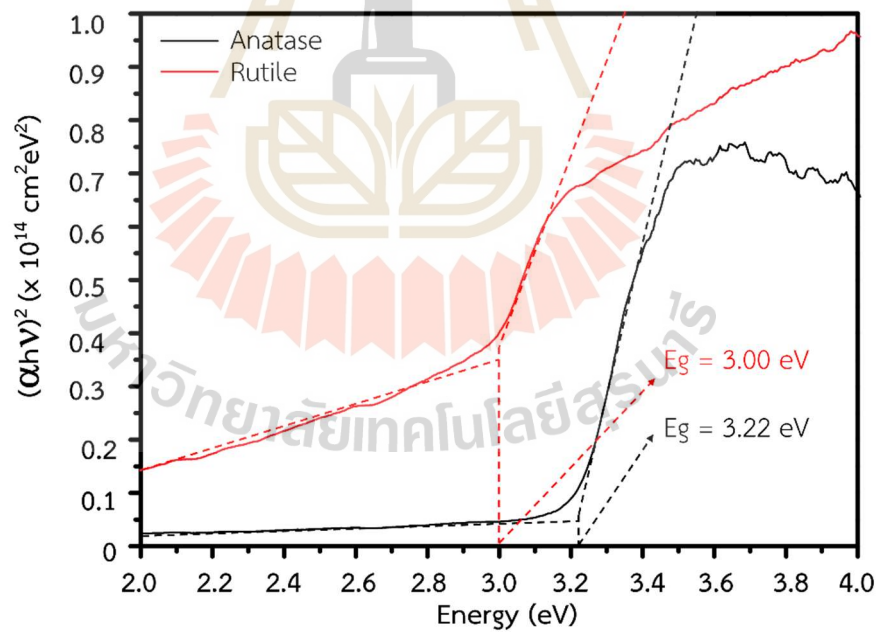


Figure 4.16 Tauc plots of rutile and anatase TiO_2 .

4.2.2 Photo-thermal CO₂ reduction activity

Rutile and anatase films on FTO substrates were cut into the size of 3 x 3 cm² and employed in photo-thermal CO₂ reduction. These films were placed in a 14.75 mL homemade gas-phase reactor, as shown in Figure 4.17a. Subsequently, CO₂ was bubbled through deionized water and passed into the reactor for 15 minutes to saturate the system with CO₂. The reactor was positioned in a water bath as shown in Figure 4.17b to maintain specific temperatures (25, 60, and 80 °C) before irradiating with a wavelength of 370 nm from an LED light source for 6 hours. The gas was sampled and analyzed using gas chromatography after 6 hours of reaction time. Control experiments were conducted under similar conditions without catalysts, and no product was detected.

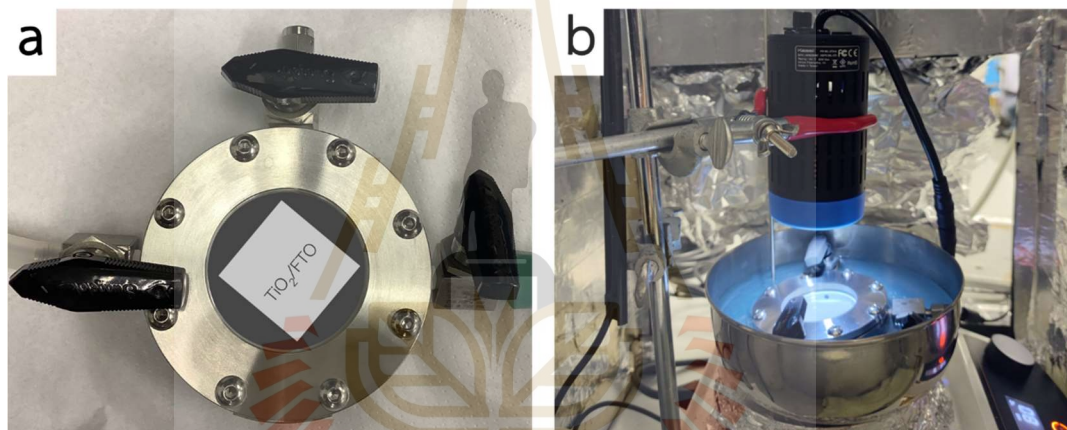


Figure 4.17 a) Homemade gas-phase reactor and b) the irradiation set up.

CO and CH₄ were the products observed from the reaction, as shown in Figure 4.18. The distinct phases of TiO₂ exhibited varying product selectivity. Anatase TiO₂ generated only CO and the CO amounts were 137.07 and 404.69 μmolm⁻² at 60 and 80 °C, respectively. No reaction occurred at 25 °C. In contrast, CH₄ was only observed when the rutile TiO₂ was used as a catalyst. Rutile yielded CO amounts of 114.88, 169.70, and 999.98 μmolm⁻² and CH₄ amounts of 0, 465.57, and 1187.27 μmolm⁻² at the reaction temperatures of 25, 60, and 80 °C, respectively.

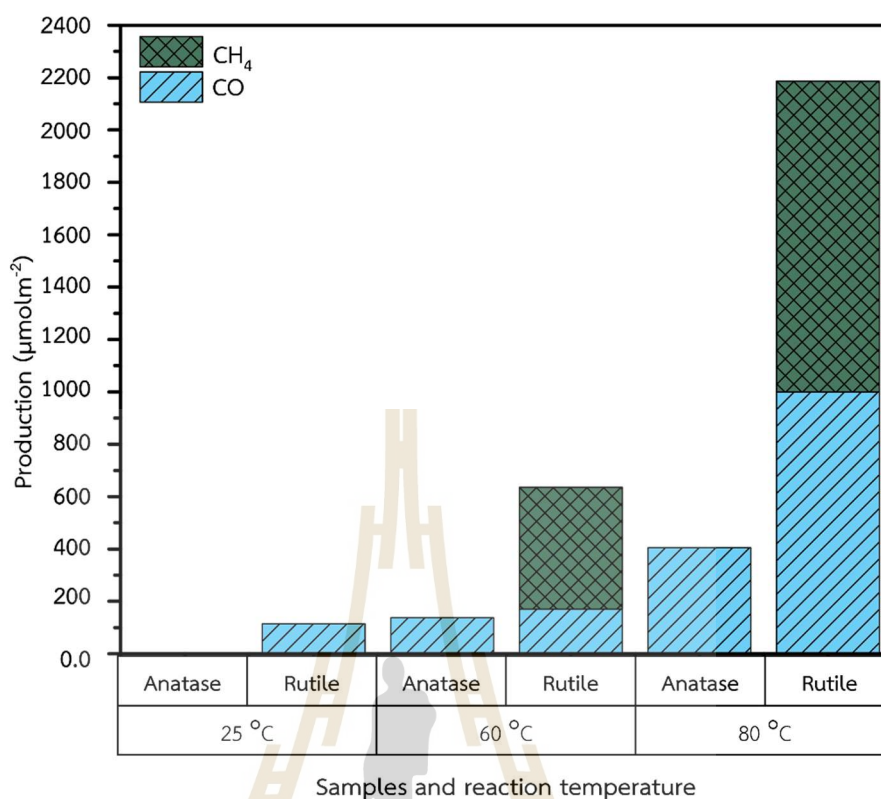


Figure 4.18 Products from photo-thermal CO₂ reduction using rutile and anatase TiO₂ catalysts under 370 nm light irradiation for 6 h.

The varying CO₂RR performances are undeniably associated with the TiO₂ phases. Rutile TiO₂ gives higher CO production compared to anatase TiO₂. This observation could be explained using the diffuse reflectance spectra. The absorption edge of the rutile phase is at 404 nm, which could be efficiently excited by the 370 nm UV light source. In contrast, the absorption edge of the anatase phase is at 377 nm, making it less excitable than the rutile phase. As a result, the charge carriers of the rutile phase for reducing CO₂ molecules would be higher. Furthermore, the anatase phase's band gap is larger, which could lead to faster charge recombination. Consequently, the possibility of CO₂ molecule reduction was diminished.

The different reaction pathways for CO₂RR in rutile and anatase TiO₂ might lead to the observed differences in selectivity. For anatase TiO₂, the reduction of CO₂ mainly results in the formation of CO. This might be attributed to the favored formation of a CO₂⁻ intermediate via a single-electron transfer, followed by a proton-coupled electron transfer (PCET) process that generates CO and a hydroxide ion (OH⁻) from adsorbed water molecules (Gagliardi et al., 2010; Wang et al., 2020). In the case of rutile TiO₂, since the adsorption energy was chemisorption, CO₂ molecules became

bent after adsorption occurred (Kovačič et al., 2022). Consequently, CO₂ molecules were more easily broken down to form CO molecules (Warren, Tronic, and Mayer, 2010; Yin et al., 2016). In addition, the formation of CH₄ indicates that multiple PCET steps were involved in the reaction mechanism. Since the adsorption energy of rutile TiO₂ is higher than anatase TiO₂, the CO molecules could remain adsorbed longer, facilitating the CO molecules to be further reduced through additional PCET steps. Therefore, rutile TiO₂ could produce both CO and CH₄.

The effects of reaction temperature were considered. The CO₂RR products increased with reaction temperature. However, the reaction temperature affected kinetics rather than reaction pathways. As the classical collision theory predicted, the increase in reaction temperature enhanced the probability of collisions between CO₂ molecules and the TiO₂ surface (Christov, 2012; Indrakanti, Kubicki, and Schobert, 2009). High reaction temperature could consequently boost the chemisorption of CO₂ molecules on the TiO₂ surface. In addition, the PCET process is more efficient at elevated temperatures than at room temperature, leading to further improved CO₂RR performance.

Moreover, the desorption of products after the reaction is completed should also be considered. It is well-known that product desorption from the catalyst surface increases with reaction temperature. Consequently, new CO₂ molecules can be adsorbed onto the TiO₂ surface after the reaction occurs at higher reaction temperatures (Li et al., 2021). The combination of increased kinetic energy and enhanced product desorption dramatically improves CO₂RR performance. A control experiment without irradiation was conducted, and no product was observed when using only heat as the energy source.

To further investigate the roles of heat energy, additional experiments were performed. The wavelength of 370 nm, UV radiation, was combined with various wavelengths to create a dual-wavelength system for catalyst excitation. The relative CO production could be obtained from the relative peak area of CO in GC chromatograms. Figure 4.19 displays the relative CO production using anatase TiO₂ as the catalyst irradiated by different dual wavelengths. The relative CO production, obtained by irradiating with dual wavelengths combining 370 nm and visible light, 465, 520, or 630 nm, did not exhibit significant differences. Interestingly, the dual-wavelength system combining 370 nm and 870 nm (infrared radiation) increases CO production. The infrared radiation introduced heat into the system and raised the reaction temperature resulting in higher CO₂RR performance. The findings confirm that

the reaction temperature acted as light assistance rather than an independent energy source for TiO₂ excitation.

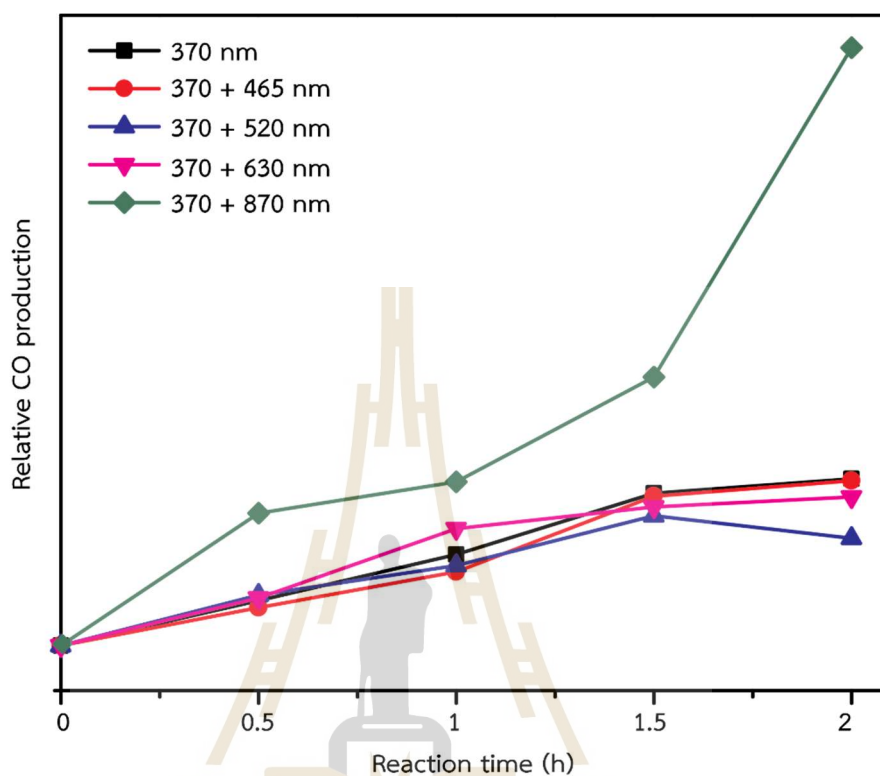


Figure 4.19 Relative CO production of different dual wavelengths using anatase as a catalyst.

The effect of water on CO₂RR was investigated. Water molecules in the system usually compete with CO₂ molecules for adsorption on the TiO₂ surface (Klyukin and Alexandrov, 2017). Therefore, a system with high humidity, implying high water content, exhibits low CO₂ adsorption. In this experiment, CO₂ was bubbled through DI water to introduce water molecules into the system. The humidity could be controlled by adjusting the temperature of the DI water, meaning that higher DI water temperatures result in higher water content in the system. In the study, CO₂ was bubbled through DI water at 25 °C and 45 °C. Figure 4.20 shows the relative CO production of anatase with different DI water temperatures after 2 h of reaction time. The results indicate that CO production significantly decreased with high water content in the system (45 °C of DI water temperature), demonstrating less CO₂ reduction. This investigation suggests that CO₂ adsorption on the TiO₂ surface is critical in CO₂RR. In addition, water is also an important factor because water serves as a critical hole

scavenger and H^+ source (Moustakas, Lorenz, Dilla, Peppel, and Strunk, 2021). Thus, the optimal water content for the system should be investigated further.

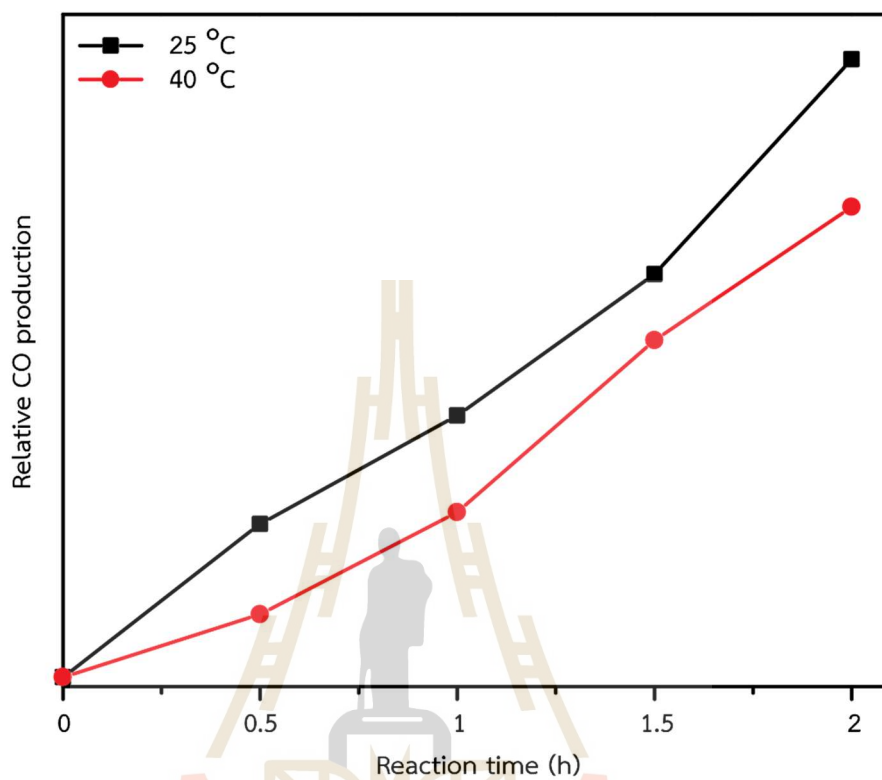


Figure 4.20 Relative CO production of different water temperatures using anatase TiO_2 as a catalyst.

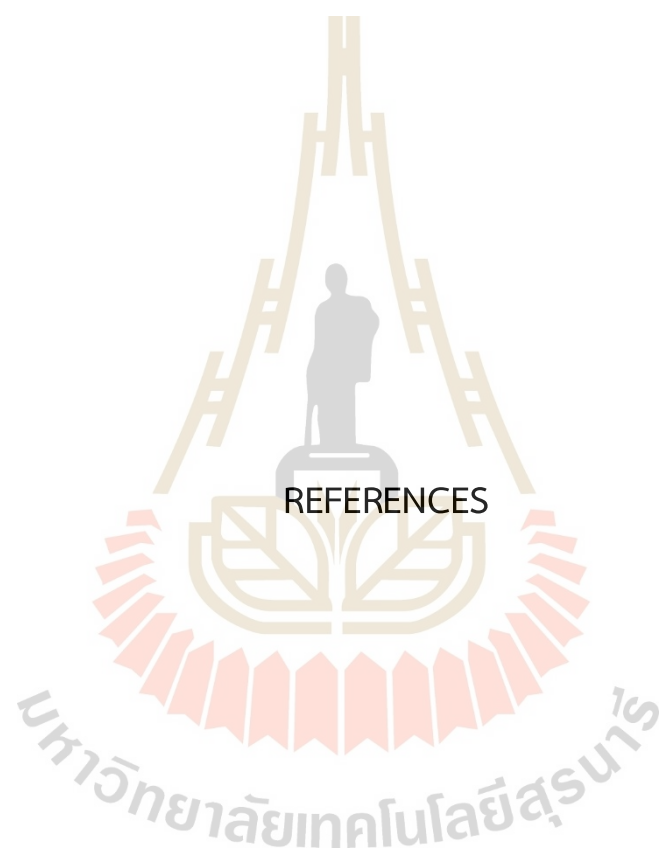
CHAPTER V

CONCLUSIONS

TiO₂ is widely recognized as a promising material for practical applications in photocatalysis. However, it faces several challenges, such as its wide band gap (3.0 – 3.2 eV), fast charge recombination, low charge carrier transportation, and high reusability costs. In this study, Facet controlled TiO₂-based catalysts were successfully grown on FTO substrates using a facile hydrothermal method for applications in photoelectrochemical and photochemical reactions.

For PEC water splitting, anatase films with different facet ratios of {101}-{001} and {010}-{001} facet pairs were used as photoanodes. The results demonstrate that controlling the facet ratio can improve the PEC water splitting performance. Films with a higher percentage of the {001} facet, particularly in the case of the {101}-{001} facet pair, exhibit higher photocurrents and incident photon-to-current efficiency. This observation can be attributed to the high surface energy and oxidation power of {001} facet. Surprisingly, the {010}-{001} facet pair, despite having the lowest percentage of the {001} facet, shows the best PEC water splitting performance. The total calculated electron affinity plays a crucial role in this phenomenon. The calculated electron affinities for each facet are 4.384, 3.193, and 2.807 for {101}, {001}, and {010} facets, respectively. The film with the highest {010} facet percentage possesses the lowest electron affinity, facilitating convenient electron transfer from the photoanode to the cathode. Moreover, conductive atomic force microscopy measurements indicate the highest adhesive force for the {010}-{001} facet pair with the lowest {001} facet. This implies that it can absorb more water molecules on its surface, which can be effectively oxidized by holes. The combination of electron affinity and water adsorption ability of the films may effectively reduce electron-hole recombination, resulting in the highest photocurrent in the case of the {010}-{001} facet pair with the lowest {001} facet percentage. Additionally, the films exhibit excellent stability, with only a slight drop in photocurrent after 6 hours of irradiation. Although the photocurrent may still be insufficient for practical applications, this study provides valuable insights for future photoanode fabrication.

In the photochemical application of CO₂ reduction, {110}-{001} rutile TiO₂ was chosen over {101}-{001} anatase TiO₂ due to its CO₂ adsorption ability. {110}-{001} rutile TiO₂ exhibits a higher CO₂ reduction rate than anatase TiO₂, which is likely influenced by CO₂ adsorption and the subsequent reaction pathways. Rutile TiO₂ has a higher CO₂ adsorption energy, leading to the further reduction of CO molecules to CH₄ through multiple proton coupled electron transfer steps. On the other hand, anatase TiO₂ releases CO molecules after their formation, resulting in 100% selectivity for CO production. The significantly higher CO₂ reduction performance of rutile TiO₂ can also be attributed to its lower band gap than anatase TiO₂. This lower band gap enables rutile to absorb light efficiently and generate charge carriers, enhancing its CO₂ reduction capabilities. When it comes to reaction temperature, an increase in temperature leads to an increase in CO₂ reduction products, but the selectivity remains unchanged. This indicates that the reaction temperature primarily affects the kinetics rather than the reaction pathways. According to the classical collision theory, elevated temperatures enhance the probability of collisions between CO₂ molecules and the TiO₂ surface, promoting CO₂ chemisorption on the TiO₂ surface. Furthermore, the multiple proton coupled electron transfer process is more efficient at higher temperatures, contributing to improved CO₂ reduction performance. Additionally, the combination of UV and infrared radiation in a dual-wavelength system, particularly at 870 nm, which introduces heat into the system, significantly increases CO production. This suggests that the reaction temperature acts as a light assistance rather than an independent energy source for TiO₂ excitation. While CO₂ adsorption on the TiO₂ surface plays a critical role in CO₂ reduction, water is also important as a hole scavenger and H⁺ source. Therefore, controlling the TiO₂ phase, water content, and reaction temperature are promising strategies for enhancing the performance of TiO₂-based photo-thermal CO₂ reduction devices. Future studies can focus on developing more efficient methods for controlling these factors to optimize the CO₂ reduction process further.



REFERENCES

REFERENCES

- Agreement, P. (2015). *Paris agreement*. Paper presented at the Report of the Conference of the Parties to the United Nations Framework Convention on Climate Change (21st Session, 2015: Paris). Retrived December, 2015.
- Allan, R. P., Hawkins, E., Bellouin, N., and Collins, B. (2021). IPCC, 2021: summary for Policymakers. *Cambridge University Press & Assessment, Cambridge, England*, pp. 3-32. (In press).
- Bakardjieva, S., Šubrt, J., Štengl, V., Dianež, M. J., and Sayagues, M. J. (2005). Photoactivity of anatase–rutile TiO₂ nanocrystalline mixtures obtained by heat treatment of homogeneously precipitated anatase. *Applied Catalysis B: Environmental*, 58(3-4), 193-202.
- Barber, J., and Tran, P. D. (2013). From natural to artificial photosynthesis. *Journal of The Royal Society Interface*, 10(81), 20120984.
- Barnard, A., and Curtiss, L. (2005). Prediction of TiO₂ nanoparticle phase and shape transitions controlled by surface chemistry. *Nano Letters*, 5(7), 1261-1266.
- Barnes, P. R., Miettunen, K., Li, X., Anderson, A. Y., Bessho, T., Gratzel, M., and O'Regan, B. C. (2013). Interpretation of optoelectronic transient and charge extraction measurements in dye-sensitized solar cells. *Advanced Materials*, 25(13), 1881-1922.
- Butburee, T., Bai, Y., Wang, H., Chen, H., Wang, Z., Liu, G., . . . Wang, L. (2018). 2D porous TiO₂ single-crystalline nanostructure demonstrating high photo-electrochemical water splitting performance. *Advanced Materials*, 30(21), 1705666.
- Butburee, T., Kotchasarn, P., Hirunsit, P., Sun, Z., Tang, Q., Khemthong, P., . . . Wang, H. (2019). New understanding of crystal control and facet selectivity of titanium dioxide ruling photocatalytic performance. *Journal of Materials Chemistry A*, 7(14), 8156-8166.
- Cao, M.-q., Liu, K., Zhou, H.-m., Li, H.-m., Gao, X.-h., Qiu, X.-q., and Liu, M. (2019). Hierarchical TiO₂ nanorods with a highly active surface for photocatalytic CO₂ reduction. *Journal of Central South University*, 26(6), 1503-1509.

- Chamtouri, M., Kenens, B., Aubert, R., Lu, G., Inose, T., Fujita, Y., . . . Uji-i, H. (2017). Facet-dependent diol-induced density of states of anatase TiO₂ crystal surface. *ACS Omega*, 2(7), 4032-4038.
- Chen, W.-H., and Chen, C.-Y. (2020). Water gas shift reaction for hydrogen production and carbon dioxide capture: A review. *Applied Energy*, 258, 114078.
- Cho, I. S., Chen, Z., Forman, A. J., Kim, D. R., Rao, P. M., Jaramillo, T. F., and Zheng, X. (2011). Branched TiO₂ nanorods for photoelectrochemical hydrogen production. *Nano Letters*, 11(11), 4978-4984.
- Christov, S. G. (2012). *Collision theory and statistical theory of chemical reactions* (Vol. 18): Springer Science & Business Media.
- Chu, S., Yan, X., Choi, C., Hong, S., Robertson, A. W., Masa, J., . . . Sun, Z. (2020). Stabilization of Cu⁺ by tuning a CuO-CeO₂ interface for selective electrochemical CO₂ reduction to ethylene. *Green Chemistry*, 22(19), 6540-6546.
- Chu, X., Mao, L., Johnson, O., Li, K., Phan, J., Yin, Q., . . . Zhang, Y. (2019). Exploration of TiO₂ nanoparticle mediated microdynamic therapy on cancer treatment. *Nanomedicine: Nanotechnology, Biology and Medicine*, 18, 272-281.
- Crake, A., Christoforidis, K. C., Gregg, A., Moss, B., Kafizas, A., and Petit, C. (2019). The effect of materials architecture in TiO₂/MOF composites on CO₂ photoreduction and charge transfer. *Small*, 15(11), 1805473.
- Das, R. (2021). Artificial Photosynthesis. In *Handbook of Nanomaterials and Nanocomposites for Energy and Environmental Applications* (pp. 1143-1161): Springer.
- Ding, Y., Wei, D., He, R., Yuan, R., Xie, T., and Li, Z. (2019). Rational design of Z-scheme PtS-ZnIn₂S₄/WO₃-MnO₂ for overall photo-catalytic water splitting under visible light. *Applied Catalysis B: Environmental*, 258, 117948.
- Dinh, C.-T., Nguyen, T.-D., Kleitz, F., and Do, T.-O. (2009). Shape-controlled synthesis of highly crystalline titania nanocrystals. *ACS Nano*, 3(11), 3737-3743.
- Docampo, P., Guldin, S., Steiner, U., and Snaith, H. J. (2013). Charge transport limitations in self-assembled TiO₂ photoanodes for dye-sensitized solar cells. *The journal of physical chemistry Letters*, 4(5), 698-703.
- Dudley, B. (2018). BP statistical review of world energy. *BP Statistical Review, London, UK*, accessed Aug, 6, 2018.
- Fan, L., Xia, C., Yang, F., Wang, J., Wang, H., and Lu, Y. (2020). Strategies in catalysts and electrolyzer design for electrochemical CO₂ reduction toward C₂₊ products. *Science Advances*, 6(8), eaay3111.

- Fujishima, A., and Honda, K. (1972). Electrochemical photolysis of water at a semiconductor electrode. *Nature*, *238*(5358), 37-38.
- Gagliardi, C. J., Westlake, B. C., Kent, C. A., Paul, J. J., Papanikolas, J. M., and Meyer, T. J. (2010). Integrating proton coupled electron transfer (PCET) and excited states. *Coordination Chemistry Reviews*, *254*(21-22), 2459-2471.
- Gao, J., Zhang, H., Guo, X., Luo, J., Zakeeruddin, S. M., Ren, D., and Grätzel, M. (2019). Selective C-C coupling in carbon dioxide electroreduction via efficient spillover of intermediates as supported by operando Raman spectroscopy. *Journal of the American Chemical Society*, *141*(47), 18704-18714.
- Gogoi, D., Namdeo, A., Golder, A. K., and Peela, N. R. (2020). Ag-doped TiO₂ photocatalysts with effective charge transfer for highly efficient hydrogen production through water splitting. *International Journal of Hydrogen Energy*, *45*(4), 2729-2744.
- Hejazi, S., Mohajernia, S., Wu, Y., Andryskova, P., Zoppellaro, G., Hwang, I., . . . Schmuki, P. (2019). Intrinsic Cu nanoparticle decoration of TiO₂ nanotubes: A platform for efficient noble metal free photocatalytic H₂ production. *Electrochemistry Communications*, *98*, 82-86.
- Hisatomi, T., Kubota, J., and Domen, K. (2014). Recent advances in semiconductors for photocatalytic and photoelectrochemical water splitting. *Chemical Society Reviews*, *43*(22), 7520-7535.
- Hu, C., Zhang, X., Li, W., Yan, Y., Xi, G., Yang, H., . . . Bai, H. (2014). Large-scale, ultrathin and (001) facet exposed TiO₂ nanosheet superstructures and their applications in photocatalysis. *Journal of Materials Chemistry A*, *2*(7), 2040-2043.
- Indrakanti, V. P., Kubicki, J. D., and Schobert, H. H. (2009). Photoinduced activation of CO₂ on Ti-based heterogeneous catalysts: Current state, chemical physics-based insights and outlook. *Energy & Environmental Science*, *2*(7), 745-758.
- Jeong, H. M., Kwon, Y., Won, J. H., Lum, Y., Cheng, M. J., Kim, K. H., . . . Kang, J. K. (2020). Atomic-Scale Spacing between Copper Facets for the Electrochemical Reduction of Carbon Dioxide. *Advanced Energy Materials*, *10*(10), 1903423.
- Jeong, S., Kim, G.-M., Kang, G.-S., Kim, C., Lee, H., Kim, W.-J., . . . Lim, H. K. (2019). Selectivity modulated by surface ligands on Cu₂O/TiO₂ catalysts for gas-phase photocatalytic reduction of carbon dioxide. *The Journal of Physical Chemistry C*, *123*(48), 29184-29191.
- Jiang, M.-P., Huang, K.-K., Liu, J.-H., Wang, D., Wang, Y., Wang, X., . . . Hou, X.-Y. (2020). Magnetic-field-regulated TiO₂ {100} facets: a strategy for CC coupling in CO₂ photocatalytic conversion. *Chem*, *6*(9), 2335-2346.

- Jones, M. R., and Fyfe, P. K. (2001). Photosynthesis: New light on biological oxygen production. *Current Biology*, 11(8), R318-R321.
- Kan, M., Qian, X., Zhang, T., Yue, D., and Zhao, Y. (2017). Highly Active IrO_x Nanoparticles/Black Si Electrode for Efficient Water Splitting with Conformal TiO₂ Interface Engineering. *ACS Sustainable Chemistry & Engineering*, 5(11), 10940-10946.
- Khezri, B., Fisher, A. C., and Pumera, M. (2017). CO₂ reduction: the quest for electrocatalytic materials. *Journal of Materials Chemistry A*, 5(18), 8230-8246.
- Klyukin, K., and Alexandrov, V. (2017). CO₂ adsorption and reactivity on rutile TiO₂ (110) in water: An ab initio molecular dynamics study. *The Journal of Physical Chemistry C*, 121(19), 10476-10483.
- Kovačič, Ž., Likozar, B., and Huš, M. (2022). Electronic properties of rutile and anatase TiO₂ and their effect on CO₂ adsorption: A comparison of first principle approaches. *Fuel*, 328, 125322.
- Lan, Y., Xie, Y., Chen, J., Hu, Z., and Cui, D. (2019). Selective photocatalytic CO₂ reduction on copper–titanium dioxide: A study of the relationship between CO production and H₂ suppression. *Chemical Communications*, 55(56), 8068-8071.
- Lee, J. K., Kim, Y.-K., Choi, B. J., Chung, T.-M., and Han, J. H. (2019). SnO-decorated TiO₂ nanoparticle with enhanced photocatalytic performance for methylene blue degradation. *Applied Surface Science*, 480, 1089-1092.
- Lei, Z., Xiong, Z., Wang, Y., Chen, Y., Cao, D., Zhao, Y., . . . Zheng, C. (2018). Photocatalytic reduction of CO₂ over facet engineered TiO₂ nanocrystals supported by carbon nanofibers under simulated sunlight irradiation. *Catalysis Communications*, 108, 27-32.
- Li, C., Koenigsmann, C., Ding, W., Rudshteyn, B., Yang, K. R., Regan, K. P., . . . Schmuttenmaer, C. A. (2015). Facet-dependent photoelectrochemical performance of TiO₂ nanostructures: an experimental and computational study. *Journal of the American Chemical Society*, 137(4), 1520-1529.
- Li, C., Shang, C., Zhao, B., Zhang, G., Liu, L., Yang, W., and Chen, Z. (2022). Effect of Bimetallic Dimer-Embedded TiO₂ (101) Surface on CO₂ Reduction: The First-Principles Calculation. *Materials*, 15(7), 2538.
- Li, J., Lu, N., Quan, X., Chen, S., and Zhao, H. (2008). Facile method for fabricating boron-doped TiO₂ nanotube array with enhanced photoelectrocatalytic properties. *Industrial & Engineering Chemistry Research*, 47(11), 3804-3808.

- Li, Q., Jia, R., Shao, J., and He, Y. (2019). Photocatalytic degradation of amoxicillin via TiO₂ nanoparticle coupling with a novel submerged porous ceramic membrane reactor. *Journal of Cleaner Production*, 209, 755-761.
- Li, Z., Zhang, L., Huang, W., Xu, C., and Zhang, Y. (2021). Photothermal Catalysis for Selective CO₂ Reduction on the Modified Anatase TiO₂ (101) Surface. *ACS Applied Energy Materials*, 4(8), 7702-7709.
- Liu, G., Sun, C., Yang, H. G., Smith, S. C., Wang, L., Lu, G. Q. M., and Cheng, H.-M. (2010). Nanosized anatase TiO₂ single crystals for enhanced photocatalytic activity. *Chemical Communications*, 46(5), 755-757.
- Liu, G., Yang, H. G., Pan, J., Yang, Y. Q., Lu, G. Q., and Cheng, H.-M. (2014). Titanium dioxide crystals with tailored facets. *Chemical Reviews*, 114(19), 9559-9612.
- Liu, L., Jiang, Y., Zhao, H., Chen, J., Cheng, J., Yang, K., and Li, Y. (2016). Engineering coexposed {001} and {101} facets in oxygen-deficient TiO₂ nanocrystals for enhanced CO₂ photoreduction under visible light. *ACS Catalysis*, 6(2), 1097-1108.
- Ma, W., Xie, S., Liu, T., Fan, Q., Ye, J., Sun, F., . . . Wang, Y. (2020). Electrocatalytic reduction of CO₂ to ethylene and ethanol through hydrogen-assisted C-C coupling over fluorine-modified copper. *Nature Catalysis*, 3(6), 478-487.
- Mao, X., Zhou, R., Zhang, S., Ding, L., Wan, L., Qin, S., . . . Miao, S. (2016). High efficiency dye-sensitized solar cells constructed with composites of TiO₂ and the hot-bubbling synthesized ultra-small SnO₂ nanocrystals. *Scientific Reports*, 6(1), 1-10.
- Mi, Y., and Weng, Y. (2015). Band alignment and controllable electron migration between rutile and anatase TiO₂. *Scientific reports*, 5(1), 1-10.
- Moore, D., Heilweck, M., and Petros, P. (2021). Saving the planet with appropriate biotechnology: 1. Diagnosing the problems Salvando el planeta con biotecnología apropiada: 1. Diagnóstico de los problemas. *Mexican Journal of Biotechnology*, 6, 1-30.
- Moustakas, N. G., Lorenz, F., Dilla, M., Peppel, T., and Strunk, J. (2021). Pivotal Role of Holes in Photocatalytic CO₂ Reduction on TiO₂. *Chemistry—A European Journal*, 27(68), 17213-17219.
- Neatu, S. t., Maciá-Agulló, J. A., Concepción, P., and Garcia, H. (2014). Gold-copper nanoalloys supported on TiO₂ as photocatalysts for CO₂ reduction by water. *Journal of the American Chemical Society*, 136(45), 15969-15976.
- Ouyang, T., Ye, Y. Q., Wu, C. Y., Xiao, K., and Liu, Z. Q. (2019). Heterostructures Composed of N-Doped Carbon Nanotubes Encapsulating Cobalt and β -Mo₂C

- Nanoparticles as Bifunctional Electrodes for Water Splitting. *Angewandte Chemie International Edition*, 58(15), 4923-4928.
- Pan, J., Liu, G., Lu, G. Q., and Cheng, H. M. (2011). On the true photoreactivity order of {001}, {010}, and {101} facets of anatase TiO₂ crystals. *Angewandte Chemie International Edition*, 50(9), 2133-2137.
- Park, J. H., Kim, S., and Bard, A. J. (2006). Novel carbon-doped TiO₂ nanotube arrays with high aspect ratios for efficient solar water splitting. *Nano Letters*, 6(1), 24-28.
- Park, S.-M., Razzaq, A., Park, Y. H., Sorcar, S., Park, Y., Grimes, C. A., and In, S.-I. (2016). Hybrid Cu_xO-TiO₂ Heterostructured Composites for Photocatalytic CO₂ Reduction into Methane Using Solar Irradiation: Sunlight into Fuel. *ACS Omega*, 1(5), 868-875.
- Peng, Y., Wu, T., Sun, L., Nsanzimana, J. M., Fisher, A. C., and Wang, X. (2017). Selective electrochemical reduction of CO₂ to ethylene on nanopores-modified copper electrodes in aqueous solution. *ACS Applied Materials & Interfaces*, 9(38), 32782-32789.
- Perathoner, S., and Centi, G. (2020). Artificial leaves using sunlight to produce fuels. In *Studies in Surface Science and Catalysis* (Vol. 179, pp. 415-430): Elsevier.
- Peter, L., Hakki, A., Mendive, C., Paz, Y., Choi, W., Wark, M., . . . Ye, J. (2016). *Photocatalysis: fundamentals and perspectives*: Royal Society of Chemistry.
- Phawa, C., Prayoonpokarach, S., Sinthiptharakoon, K., Chakthranont, P., Sangkhun, W., Faungnawakij, K., and Butburee, T. (2020). Effects of matching facet pairs of TiO₂ on photoelectrochemical water splitting behaviors. *ChemCatChem*, 12(7), 2116-2124.
- Pörtner, H. O., Roberts, D. C., Adams, H., Adler, C., Aldunce, P., Ali, E., . . . Biesbroek, R. (2022). *Climate change 2022: impacts, adaptation and vulnerability*. IPCC, 2022.
- Prakash, S. (2021). Impact of Climate change on Aquatic Ecosystem and its Biodiversity: An overview. *International Journal of Biological Innovations*, 3(2).
- Roy, N., Park, Y., Sohn, Y., Leung, K. T., and Pradhan, D. (2014). Green synthesis of anatase TiO₂ nanocrystals with diverse shapes and their exposed facets-dependent photoredox activity. *ACS Applied Materials & Interfaces*, 6(19), 16498-16507.
- Roy, N., Sohn, Y., and Pradhan, D. (2013). Synergy of low-energy {101} and high-energy {001} TiO₂ crystal facets for enhanced photocatalysis. *ACS Nano*, 7(3), 2532-2540.

- Sadhu, S., and Poddar, P. (2014). Template-free fabrication of highly-oriented single-crystalline 1D-rutile TiO₂-MWCNT composite for enhanced photoelectrochemical activity. *The Journal of Physical Chemistry C*, 118(33), 19363-19373.
- Scanlon, D. O., Dunnill, C. W., Buckeridge, J., Shevlin, S. A., Logsdail, A. J., Woodley, S. M., . . . Parkin, I. P. (2013). Band alignment of rutile and anatase TiO₂. *Nature Materials*, 12(9), 798-801.
- Shiu, J.-W., Lan, C.-M., Chang, Y.-C., Wu, H.-P., Huang, W.-K., and Diau, E. W.-G. (2012). Size-controlled anatase titania single crystals with octahedron-like morphology for dye-sensitized solar cells. *ACS Nano*, 6(12), 10862-10873.
- Tian, F., Zhang, Y., Zhang, J., and Pan, C. (2012). Raman spectroscopy: a new approach to measure the percentage of anatase TiO₂ exposed (001) facets. *The Journal of Physical Chemistry C*, 116(13), 7515-7519.
- Vittadini, A., Selloni, A., Rotzinger, F., and Grätzel, M. (1998). Structure and energetics of water adsorbed at TiO₂ anatase {101} and {001} surfaces. *Physical Review Letters*, 81(14), 2954.
- Wang, H., Wang, Y., Guo, L., Zhang, X., Ribeiro, C., and He, T. (2020). Solar-heating boosted catalytic reduction of CO₂ under full-solar spectrum. *Chinese Journal of Catalysis*, 41(1), 131-139.
- Wang, S., Cabrero-Antonino, M., Navalón, S., Cao, C.-c., Tissot, A., Dovgaliuk, I., . . . Wang, H. (2020). A robust titanium isophthalate metal-organic framework for visible-light photocatalytic CO₂ methanation. *Chem*, 6(12), 3409-3427.
- Wang, S., Chen, H., Gao, G., Butburee, T., Lyu, M., Thaweesak, S., . . . Wang, L. (2016). Synergistic crystal facet engineering and structural control of WO₃ films exhibiting unprecedented photoelectrochemical performance. *Nano Energy*, 24, 94-102.
- Warren, J. J., Tronic, T. A., and Mayer, J. M. (2010). Thermochemistry of proton-coupled electron transfer reagents and its implications. *Chemical Reviews*, 110(12), 6961-7001.
- Wu, Q., Liu, M., Wu, Z., Li, Y., and Piao, L. (2012). Is photooxidation activity of {001} facets truly lower than that of {101} facets for anatase TiO₂ crystals? *The Journal of Physical Chemistry C*, 116(51), 26800-26804.
- Wu, T., Zhu, X., Xing, Z., Mou, S., Li, C., Qiao, Y., . . . Zhang, Y. (2019). Greatly improving electrochemical N₂ reduction over TiO₂ nanoparticles by iron doping. *Angewandte Chemie International Edition*, 58(51), 18449-18453.

- Xia, H., Wang, Y., Lin, J., and Lu, L. (2012). Hydrothermal synthesis of MnO₂/CNT nanocomposite with a CNT core/porous MnO₂ sheath hierarchy architecture for supercapacitors. *Nanoscale Research Letters*, 7(1), 33.
- Xu, C., Huang, W., Li, Z., Deng, B., Zhang, Y., Ni, M., and Cen, K. (2018). Photothermal coupling factor achieving CO₂ reduction based on palladium-nanoparticle-loaded TiO₂. *ACS Catalysis*, 8(7), 6582-6593.
- Xu, M., Kong, L., Zhou, W., and Li, H. (2007). Hydrothermal synthesis and pseudocapacitance properties of α -MnO₂ hollow spheres and hollow urchins. *The Journal of Physical Chemistry C*, 111(51), 19141-19147.
- Yaemsunthorn, K., Kobielski, M., and Macyk, W. (2021). TiO₂ with tunable anatase-to-rutile nanoparticles ratios: how does the photoactivity depend on the phase composition and the nature of photocatalytic reaction? *ACS Applied Nano Materials*, 4(1), 633-643.
- Yan, L., Chen, H., and Jing, C. (2019). TiO₂ facets shaped by concentration-dependent surface diffusion of dopamine. *The Journal of Physical Chemistry Letters*, 10(5), 898-903.
- Yang, H., Lin, Q., Zhang, C., Yu, X., Cheng, Z., Li, G., . . . Liu, J. (2020). Carbon dioxide electroreduction on single-atom nickel decorated carbon membranes with industry compatible current densities. *Nature Communications*, 11(1), 1-8.
- Yang, H. G., Sun, C. H., Qiao, S. Z., Zou, J., Liu, G., Smith, S. C., . . . Lu, G. Q. (2008). Anatase TiO₂ single crystals with a large percentage of reactive facets. *Nature*, 453(7195), 638-641.
- Ye, L., Liu, J., Tian, L., Peng, T., and Zan, L. (2013). The replacement of {1 0 1} by {0 1 0} facets inhibits the photocatalytic activity of anatase TiO₂. *Applied Catalysis B: Environmental*, 134, 60-65.
- Ye, L., Mao, J., Liu, J., Jiang, Z., Peng, T., and Zan, L. (2013). Synthesis of anatase TiO₂ nanocrystals with {101},{001} or {010} single facets of 90% level exposure and liquid-phase photocatalytic reduction and oxidation activity orders. *Journal of Materials Chemistry A*, 1(35), 10532-10537.
- Yin, W.-J., Wen, B., Bandaru, S., Krack, M., Lau, M., and Liu, L.-M. (2016). The effect of excess electron and hole on CO₂ adsorption and activation on rutile (110) surface. *Scientific Reports*, 6(1), 23298.
- Yin, W.-J., Wen, B., Ge, Q., Li, X.-B., Teobaldi, G., and Liu, L.-M. (2020). Activity and selectivity of CO₂ photoreduction on catalytic materials. *Dalton Transactions*, 49(37), 12918-12928.

- Yoro, K. O., and Daramola, M. O. (2020). CO₂ emission sources, greenhouse gases, and the global warming effect. In *Advances in Carbon Capture* (pp. 3-28): Elsevier.
- Yu, H., Pan, J., Bai, Y., Zong, X., Li, X., and Wang, L. (2013). Hydrothermal synthesis of a crystalline rutile TiO₂ nanorod based network for efficient dye-sensitized solar cells. *Chemistry–A European Journal*, 19(40), 13569-13574.
- Yu, J., Low, J., Xiao, W., Zhou, P., and Jaroniec, M. (2014). Enhanced photocatalytic CO₂-reduction activity of anatase TiO₂ by coexposed {001} and {101} facets. *Journal of the American Chemical Society*, 136(25), 8839-8842.
- Zandalinas, S. I., Fritschi, F. B., and Mittler, R. (2021). Global warming, climate change, and environmental pollution: recipe for a multifactorial stress combination disaster. *Trends in Plant Science*, 26(6), 588-599.
- Zhang, H., Wang, W., Zhao, H., Zhao, L., Gan, L.-Y., and Guo, L.-H. (2018). Facet-dependent interfacial charge transfer in Fe (III)-grafted TiO₂ nanostructures activated by visible light. *ACS Catalysis*, 8(10), 9399-9407.
- Zhang, P., Lu, X. F., Nai, J., Zang, S. Q., and Lou, X. W. (2019). Construction of hierarchical Co-Fe oxyphosphide microtubes for electrocatalytic overall water splitting. *Advanced Science*, 6(17), 1900576.
- Zhao, Z., Li, Z., and Zou, Z. (2010). Surface properties and electronic structure of low-index stoichiometric anatase TiO₂ surfaces. *Journal of Physics: Condensed Matter*, 22(17), 175008.
- Zheng, Y., Vasileff, A., Zhou, X., Jiao, Y., Jaroniec, M., and Qiao, S.-Z. (2019). Understanding the roadmap for electrochemical reduction of CO₂ to multi-carbon oxygenates and hydrocarbons on copper-based catalysts. *Journal of the American Chemical Society*, 141(19), 7646-7659.
- Zheng, Z., Huang, B., Lu, J., Qin, X., Zhang, X., and Dai, Y. (2011). Hierarchical TiO₂ microspheres: synergetic effect of {001} and {101} facets for enhanced photocatalytic activity. *Chemistry–A European Journal*, 17(52), 15032-15038.

CURRICULUM VITAE

Name Chaiyasit Phawa
Date of Birth 2 August 1993
Place of Birth Nakhon Phanom, Thailand

Education

2012 – 2015 B.Sc. in Chemistry (1st Class Honors), Khon Kaen University, Khon Kean, Thailand
2016 – 2022 Ph.D. candidate in Chemistry, Suranaree University of Technology, Nakhon Ratchasima, Thailand

Scholarship

2012 – 2020 Science Achievement Scholarship of Thailand, SAST

Publications

1. **Phawa, C.**, Prayoonpokarach, S., Sinthiptharakoon, K., Chakthranont, P., Sangkhun, W., Faungnawakij, K., and Butburee, T. (2020). Effects of matching facet pairs of TiO₂ on photoelectrochemical water splitting behaviors. *ChemCatChem*, 12(7), 2116-2124.
2. Butburee, T., Chakthranont, P., **Phawa, C.**, and Faungnawakij, K. (2020). Beyond artificial photosynthesis: prospects on photobiorefinery. *ChemCatChem*, 12(7), 1873-1890.
3. Sangkhun, W., Ponchai, J., **Phawa, C.**, Pengsawang, A., Faungnawakij, K., and Butburee, T. (2022). Race on high-loading metal single atoms and successful preparation strategies. *ChemCatChem*, 14(2), e202101266.
4. Bunrit, A., Butburee, T., Liu, M., Huang, Z., Meeporn, K., **Phawa, C.**, ... Wang, F. (2022). Photo-thermo-dual catalysis of levulinic acid and levulinate ester to γ -valerolactone. *ACS Catalysis*, 12(3), 1677-1685.
5. Butburee, T., Ponchai, J., Meeporn, K., **Phawa, C.**, Chakthranont, P., Khemthong, P., ... Pennycook, S. (2022). New folding 2D-layered nitro-oxygenated carbon containing ultra high-loading copper single atoms. *Small*, 18(51), 2204767.